

The dynamics of spanwise vorticity perturbations in homogeneous viscoelastic shear flow

Jacob Page¹ and Tamer A. Zaki^{1,2,†}

¹Mechanical Engineering, Imperial College London, London SW7 2AZ, UK

²Mechanical Engineering, Johns Hopkins University, Baltimore, MD 21218, USA

(Received 18 December 2014; revised 16 April 2015; accepted 24 June 2015;
first published online 20 July 2015)

The viscoelastic analogue to the Newtonian Orr amplification mechanism is examined using linear theory. A weak, two-dimensional Gaussian vortex is superposed onto a uniform viscoelastic shear flow. Whilst in the Newtonian solution the spanwise vorticity perturbations are simply advected, the viscoelastic behaviour is markedly different. When the polymer relaxation rate is much slower than the rate of deformation by the shear, the vortex splits into a new pair of co-rotating but counter-propagating vortices. Furthermore, the disturbance exhibits a significant amplification in its spanwise vorticity as it is tilted forward by the shear. Asymptotic solutions for an Oldroyd-B fluid in the limits of high and low elasticity isolate and explain these two effects. The splitting of the vortex is a manifestation of vorticity wave propagation along the tensioned mean-flow streamlines, while the spanwise vorticity growth is driven by the amplification of a polymer torque perturbation. The analysis explicitly demonstrates that the polymer torque amplifies as the disturbance becomes aligned with the shear. This behaviour is opposite to the Orr mechanism for energy amplification in Newtonian flows, and is therefore labelled a ‘reverse-Orr’ mechanism. Numerical evaluations of vortex evolutions using the more realistic FENE-P model, which takes into account the finite extensibility of the polymer chains, show the same qualitative behaviour. However, a new form of stress perturbation is established in regions where the polymer is significantly stretched, and results in an earlier onset of decay.

Key words: non-Newtonian flows, viscoelasticity

1. Introduction

Viscoelasticity often introduces counter-intuitive behaviour into the flow dynamics across a wide range of regimes. Perhaps the most well-known effect is the substantial drag reduction achieved by the addition of small amounts of polymer to turbulent flows (White & Mungal 2008). At these low concentrations, the polymer is found to suppress the formation of the near-wall streamwise vortices, resulting in weaker streaks and a reduction in skin friction. A similar trend is observed in the simplified linear problem of roll–streak interaction in laminar Couette flow (Page & Zaki 2014).

† Email address for correspondence: t.zaki@jhu.edu

The influence of polymer additives on spanwise vortical structures has also been noted in the literature; for example, they alter the linear instabilities of free-shear layers (Azaiez & Homsy 1994; Rallison & Hinch 1995; Ray & Zaki 2014) and can suppress the von Kármán vortex street downstream of a cylinder (Cadot & Kumar 2000). In moderate Reynolds number channel flow, where a Newtonian fluid would remain laminar, viscoelastic fluids sustain a chaotic elasto-inertial state dominated by two-dimensional structures (Samanta *et al.* 2013). Furthermore, in high Reynolds number drag-reduced flows, the polymer has a damping effect on hairpin vortices (Kim *et al.* 2007). Motivated by the importance of spanwise vorticity in shear flows and the success of linear theory in clarifying the roll–streak dynamics, we examine the impact of viscoelasticity on the linear evolution of a two-dimensional vortical disturbance in homogeneous shear.

1.1. Disturbance amplification in viscoelastic flows

Transient growth of small disturbances in viscoelastic shear flows has been the focus of recent studies, most of which have focused on streamwise elongated perturbations. For example, Jovanović & Kumar (2010, 2011) demonstrated that significant energy amplification is possible even in the absence of inertia. This property therefore provides a potential pathway to inertialess elastic turbulence (Groisman & Steinberg 2000; Pan *et al.* 2013). The zero Reynolds number growth is due to polymer stretch (Kupferman 2005; Doering, Eckhardt & Schumacher 2006), whereby a streamwise force is generated as the polymer is deformed by the shear. The flow response takes the form of streamwise streaks, similar in appearance to inertial transient growth in Newtonian fluids. Further studies have addressed the influence of weak inertia (Page & Zaki 2014) and finite polymer extensibility (Lieu, Jovanović & Kumar 2013) on this elastic growth. In inertia-dominated flows, Hoda, Jovanović & Kumar (2008, 2009) introduced stochastic forcing in the linear equations for an Oldroyd-B fluid and demonstrated that viscoelasticity enhances the energy density of the response. Based on their energy analysis, Hoda *et al.* (2009) were able to attribute this growth to polymer stretch. The relation between this inertial and the aforementioned elastic growth was established by Page & Zaki (2014). That work examined the streak response to a decaying streamwise vortex, and demonstrated a dependence on the ratio of the relaxation time to the disturbance diffusion time scale in the solvent. If relaxation is relatively fast, the polymer behaves like an additional solvent and a Newtonian behaviour is recovered. If relaxation is comparatively slow, the dynamics in the solvent and polymer effectively decouple and large elastic growth can be attained. Finally, when the time scales are commensurate, the system supports the propagation of vorticity waves, and the streaks can re-energize.

In contrast to the above studies, which focused on streamwise independent perturbations, Zhang *et al.* (2013) studied the influence of fluid elasticity on the amplification of oblique disturbances. For subcritical, weakly elastic channel flow of a FENE-P fluid, the optimal growth of oblique disturbances was found to be attenuated relative to the Newtonian case. Another instance where three-dimensional disturbances have received attention is the study of elliptic flows. Whilst in the Newtonian case the unstable waves are three-dimensional (Bayly 1986), Lagnado & Simmen (1993) demonstrated that the instability becomes predominantly two-dimensional at high elasticity. The instability mechanism was later explained by Haj-Hariri & Homsy (1997), and is driven by the rotation of the perturbation wavevector. The above linear studies have recently been complemented by the first direct numerical simulations

(DNS) of the full transition process in an inertia-dominated viscoelastic channel flow at subcritical Reynolds number (Agarwal, Brandt & Zaki 2014). Starting from an initially localized velocity perturbation, the disturbance evolution was tracked from an early linear amplification phase through to a turbulent state similar to the maximum drag reduction (MDR) regime. Their analysis of the energy equation demonstrated that the polymer tends to resist, or damp, the initial vorticity.

1.2. Polymeric turbulent flows

It is generally accepted that the phenomenon of drag reduction through the addition of polymer to a Newtonian flow is associated with a large extensional viscosity in the buffer layer (Hinch 1977; White & Mungal 2008). The exact mechanism remains a subject of debate, but there is substantial experimental and numerical evidence that the presence of stretched polymers in this region disrupts the self-sustaining cycle of near-wall turbulence. For example, experiments by Tiederman and coworkers (Luchik & Tiederman 1988; Walker & Tiederman 1990; Harder & Tiederman 1991) found that the frequency of bursting events decreases in dilute solutions, and that the magnitude of wall-normal velocity fluctuations is reduced. The same observation has also been made in connection with numerical simulations of drag-reduced flows (Min *et al.* 2003; Ptasinski *et al.* 2003; Dubief *et al.* 2004), and motivates an examination of the effects of the polymer on intermittent events and individual flow structures rather than relying solely on a statistical description.

Studies of intermittency in direct numerical simulations of polymeric turbulence have shown that viscoelasticity promotes prolonged periods of ‘hibernating turbulence’, a state of low drag which is also present to a lesser extent in Newtonian flows (Xi & Graham 2010, 2012). These results offer a possible explanation for the universality of MDR (Graham 2014). An important flow feature common to both drag-reduced and MDR flows is the near-wall streamwise vortices. The polymer tends to damp these structures which generate the buffer-layer streaks (Dimitropoulos *et al.* 2001; Dubief *et al.* 2004, 2005).

The influence of polymers on spanwise vortical structures, such as the hairpin vortices found above the buffer layer, has received less attention. One notable exception is the study by Kim *et al.* (2007). Using conditional averaging, those authors were able to extract flow structures associated with ejection events. Their analysis explicitly demonstrated that a streamwise polymer torque tends to oppose the rotation of streamwise vortices in the buffer layer. More relevant to the present study is their observation that a resistive torque is also established around the head of the hairpin vortices: the polymer tends to oppose spanwise vortical motions.

Recent simulations and experiments at near-critical Reynolds numbers also highlight the significance of spanwise vortical structures. Samanta *et al.* (2013) focused on relatively high polymer concentrations (~500 ppm) in a moderate Reynolds number regime where the equivalent Newtonian flow would be laminar. They reported that a chaotic state is sustained through a combination of elastic instabilities and inertial effects – a state which they termed elasto-inertial turbulence. The dominant flow structures are different from the rolls and streaks that are prevalent in transitional and turbulent flows. Instead, spanwise ‘sheets’, where the polymer is significantly stretched, are formed and align with the mean shear. These sheets of polymer conformation are accompanied by cylindrical spanwise structures of rotational and extensional flow (Dubief, Terrapon & Soria 2013; Terrapon, Dubief & Soria 2014). Wang *et al.* (2014) affirmed the importance of spanwise independent structures in

polymeric turbulent flows, and hinted at a connection between the elasto-inertial turbulence and MDR. By applying proper orthogonal decomposition to time series of both velocity and polymer stress fields from simulations of MDR in minimal flow domains, they demonstrated that the dominant modes in the hibernating state also exhibit a sheet-like structure, with large polymer stretch occurring in thin, isolated layers.

While turbulent flows are highly nonlinear, a good deal of insight into the mechanics of energy injection into the perturbation field can be derived from linear theory. For example, the physical process governing the formation of streaks in shear flows of Newtonian fluids, or lift-up, has typically been examined in the context of linear disturbance amplification in laminar and transitional flows (Landahl 1980; Butler & Farrell 1992). The same underlying mechanism is also of central importance in the turbulent regime, where streaks of streamwise velocity are observed across a range of scales (Robinson 1991). By adapting the linear analysis for the case of a fully turbulent mean-flow profile, del Álamo & Jiménez (2006) were able to predict the dominant length scales of the streaks, in particular the outer large-scale motions that fill the channel, and also the buffer-layer streaks. A second type of transient growth operates in Newtonian flows, namely the inviscid Orr mechanism. Orr amplification can be traced to mass-conservation and therefore to the action of pressure. Unlike lift-up, the Orr mechanism favours perturbations with a streamwise dependence (Farrell 1987; Butler & Farrell 1992). A recent study by Jiménez (2013) examined the relevance of linear Orr growth to bursting events above the buffer layer in turbulent flows. There are qualitative similarities between the idealized linear behaviour and nonlinear bursting events, though it is suggested that a complete explanation also requires an instability of the buffer layer streaks.

In the present study we investigate the viscoelastic analogue of the Newtonian Orr mechanism by computing the linear evolution of a localized spanwise vortex in homogeneous, viscoelastic shear flow. The relative importance of inertia is controlled by varying the vortex length scale, and a wide range of disturbance Reynolds numbers are considered. Our work thus advances our understanding of the dynamics of linear disturbances in viscoelastic shear flows, and provides a foundation for interpreting observations from more complex nonlinear configurations such as elasto-inertial and MDR turbulence. The remainder of this paper is organized as follows. In §2 we formulate the physical problem and present the governing linear equations. For Oldroyd-B fluids these are reduced to a pair of equations for the spanwise vorticity and polymer torque. In §3 the evolution of an isolated vortex is considered for an Oldroyd-B fluid, and the limits of low and high elasticity are examined asymptotically in order to explain some of the general features of the solution. The effects of finite extensibility are examined in §4, where we compute vortex evolutions in a FENE-P fluid. Finally, conclusions are provided in §5.

2. Theoretical formulation

The viscoelasticity of a fluid is modelled in the equations of continuum mechanics through a polymeric contribution to the total stress alongside the Newtonian solvent contribution. With this addition, the mass conservation and momentum equations are

$$\frac{\partial U_j}{\partial x_j} = 0, \quad (2.1a)$$

$$\rho \left(\frac{\partial U_i}{\partial t} + U_j \frac{\partial U_i}{\partial x_j} \right) = - \frac{\partial P}{\partial x_i} + \mu_s \frac{\partial^2 U_i}{\partial x_j \partial x_j} + \mu_p \frac{\partial T_{ij}}{\partial x_j}, \quad (2.1b)$$

where $\mu_p T_{ij}$ is the polymeric stress. Our principal interest is the evolution of disturbances in dilute solutions, which are well described by the FENE-P constitutive equation (Bird, Armstrong & Hassager 1987)

$$T_{ij} = \frac{1}{\zeta} (F C_{ij} - \delta_{ij}), \tag{2.2a}$$

where ζ is a relaxation time, C_{ij} is the polymer conformation and

$$F = \frac{L^2 - 3}{L^2 - C_{kk}} \tag{2.2b}$$

is the Peterlin function – a nonlinear spring law that provides an upper bound on the extension of the polymer chains. The parameter L is related to the maximum extensibility of the polymer chains by $L^2 = L_{max}^2 + 3$, where L_{max} has been normalized by the equilibrium chain length. The polymer conformation is an ensemble average of chain orientations, $C_{ij} = (L^2/L_{max}^2) \langle r_i r_j \rangle$, where the coefficient L^2/L_{max}^2 is included so that $C_{ij} = \delta_{ij}$ in the absence of flow (Jin & Collins 2007). Much of the theoretical development in this paper will invoke the assumption of infinite extensibility, and the limit $L \rightarrow \infty$ yields $F = 1$, which is a linear spring law, or the Oldroyd-B fluid. The conformation tensor evolves according to

$$\overset{\nabla}{C}_{ij} \equiv \underbrace{\frac{\partial C_{ij}}{\partial t} + U_k \frac{\partial C_{ij}}{\partial x_k}}_{\text{advection}} - \underbrace{C_{ik} \frac{\partial U_j}{\partial x_k} - C_{kj} \frac{\partial U_i}{\partial x_k}}_{\text{stretching/distortion}} = \underbrace{-T_{ij}}_{\text{relaxation}}. \tag{2.3}$$

The base flow considered herein is a simple unbounded shear, which is one of a family of linear flows,

$$U_i(\mathbf{x}) = \Gamma_{ij} x_j, \tag{2.4}$$

where incompressibility requires that $\Gamma_{jj} = 0$. For these flows where the deformation rate is constant, the stretching of the polymers is homogeneous in space, and steady solutions for the base-state stretch are

$$T_{ij} = C_{ik} \Gamma_{jk} + C_{kj} \Gamma_{ik}. \tag{2.5}$$

The linear perturbation equations for any base flow satisfying (2.4) are derived in § 2.1, and the case of simple shear is presented in § 2.2.

2.1. Linear perturbation equations: forces and torques in Oldroyd-B fluids

When the base state (2.4) is slightly perturbed, the small disturbance evolves according to the linear equations

$$\frac{\partial u_j}{\partial x_j} = 0, \tag{2.6a}$$

$$\rho \left(\frac{\partial u_i}{\partial t} + \Gamma_{jk} x_k \frac{\partial u_i}{\partial x_j} + u_j \Gamma_{ij} \right) = -\frac{\partial p}{\partial x_i} + \mu_s \frac{\partial^2 u_i}{\partial x_j \partial x_j} + \mu_p f_i, \tag{2.6b}$$

$$\frac{\partial c_{ij}}{\partial t} + \Gamma_{kl} x_l \frac{\partial c_{ij}}{\partial x_k} = C_{ik} \frac{\partial u_j}{\partial x_k} + c_{ik} \Gamma_{jk} + C_{kj} \frac{\partial u_i}{\partial x_k} + c_{kj} \Gamma_{ik} - \tau_{ij}. \tag{2.6c}$$

The final term in the momentum equation (2.6*b*), $\mu_p f_i \equiv \mu_p \partial \tau_{ij} / \partial x_j$, is the perturbation force due to the polymer. The stress perturbations are related to perturbations in the polymer conformation by

$$\tau_{ij} = \frac{F}{\zeta} \left(c_{ij} + \underbrace{\frac{1}{L^2 - C_{ll}} C_{ij} c_{kk}}_{\mathcal{N}} \right). \tag{2.7}$$

For an Oldroyd-B fluid, $L \rightarrow \infty$, and the perturbation stress is $\tau_{ij} = c_{ij} / \zeta$. There is a direct proportionality between stretch and stress perturbations as a consequence of the linear spring law. In the more general case (2.7), the nonlinearity of the springs results in an additional type of stress perturbation, labelled \mathcal{N} . These stress perturbations are a result of the perturbation stretch bringing the polymer chains closer to or further from their maximum extensibility.

The linear perturbation equations can be simplified substantially when the finite extensibility of the polymers can be ignored. Therefore, the analysis now proceeds for the Oldroyd-B fluid, i.e. $L \rightarrow \infty$ (the discussion of finite extensibility is deferred to §4). One particularly useful feature when the mean rate of deformation, Γ_{ij} , is constant is that we need only consider the evolution of the polymer forces rather than the conformation field. This is evident by taking the divergence of (2.6*c*):

$$\frac{\partial f_i}{\partial t} + \Gamma_{jk} x_k \frac{\partial f_i}{\partial x_j} + \frac{1}{\zeta} f_i = f_j \Gamma_{ij} + T_{jk} \frac{\partial^2 u_i}{\partial x_j \partial x_k} + \frac{1}{\zeta} \frac{\partial^2 u_i}{\partial x_j \partial x_j}. \tag{2.8}$$

On the left-hand side are the linearized advection and the relaxation terms. The first term on the right-hand side represents the polymer stretch mechanism. It is similar to the vortex deformation term which appears in the linearized vorticity equation, but remains active in two-dimensional flows. The second term on the right-hand side describes the generation of polymer force due to the distortion of the mean polymer stresses by curvature in the velocity field. Taking the divergence once again yields

$$\left(\frac{\partial}{\partial t} + \Gamma_{jk} x_k \frac{\partial}{\partial x_j} + \frac{1}{\zeta} \right) \nabla \cdot \mathbf{f} = 0. \tag{2.9}$$

Therefore, an initially divergence-free polymer force field will remain so. In this work the initial disturbance is devoid of any initial polymer force and as a result $\nabla \cdot \mathbf{f} = 0$ at all times. Equation (2.9) also indicates that the perturbation pressure field is not directly influenced by the polymer forces since the source term due to the polymer in the pressure Poisson equation vanishes. Instead, the polymer has an indirect impact via its influence on the velocity field.

It is instructive to further manipulate the linear equations into a vorticity–torque system. Upon taking the curl of (2.6*b*) we obtain

$$\frac{\partial \omega_i}{\partial t} + \Gamma_{jk} x_k \frac{\partial \omega_i}{\partial x_j} = \underbrace{\omega_j \Gamma_{ij} + \Omega_j \frac{\partial u_i}{\partial x_j}} + \nu_s \frac{\partial^2 \omega_i}{\partial x_j \partial x_j} + \nu_p \chi_i, \tag{2.10}$$

where $\boldsymbol{\omega} \equiv \nabla \wedge \mathbf{u}$ is the perturbation vorticity vector and $\Omega_i \equiv \epsilon_{ijk} \Gamma_{kj}$ is the constant mean vorticity. The terms identified by the underbrace together represent the linearized vortex deformation term, and they vanish for purely spanwise vorticity perturbations in two-dimensional flows. We have also introduced the quantity $\boldsymbol{\chi} \equiv \nabla \wedge \mathbf{f}$, which we

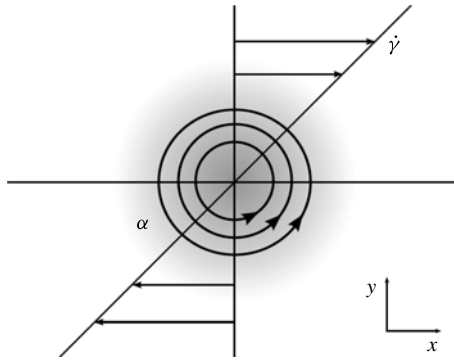


FIGURE 1. Schematic of the model problem. The background flow is simple shear, $U = \dot{\gamma}y$. A weak spanwise vortex of rotation rate α is superposed at the origin.

label the ‘polymer torque’. This torque is related to the true torque exerted on the fluid by the polymer stresses (see § A.1) in the same way that the vorticity is related to the angular momentum of a fluid element. The polymer torque is in part dependent on the vorticity history, and its evolution follows from taking the curl of (2.8):

$$\frac{\partial \chi_i}{\partial t} + \Gamma_{jk} x_k \frac{\partial \chi_i}{\partial x_j} + \frac{1}{\zeta} \chi_i = \underbrace{\chi_j \Gamma_{ij} + \Omega_j \frac{\partial f_i}{\partial x_j} + 2\epsilon_{ijk} \frac{\partial}{\partial x_j} (\Gamma_{kl} f_l)}_{\text{kinematic torque}} + T_{jk} \frac{\partial^2 \omega_i}{\partial x_j \partial x_k} + \frac{1}{\zeta} \frac{\partial^2 \omega_i}{\partial x_j \partial x_j}. \quad (2.11)$$

The expression identified with an underbrace contains terms analogous to the linearized vorticity equation (2.10). Similar to vortex deformation in (2.10), they vanish when we consider purely spanwise vorticity perturbations to two-dimensional flows. However, the final term, $2\epsilon_{ijk} \partial (\Gamma_{kl} f_l) / \partial x_j = 2\nabla \wedge (\Gamma \mathbf{f})$, remains. It constitutes a kinematic torque amplification mechanism which will be examined in detail.

Equations (2.10) and (2.11) provide a complete description of the disturbance evolution. Casting them in terms of vorticity and torque is particularly advantageous due to the present focus on spanwise vorticity perturbations. Furthermore, the notion of polymer torque is conceptually beneficial. Its importance and utility have been alluded to previously in the literature (Kumar & Homsy 1999; Kim *et al.* 2007; Jovanović & Kumar 2011), and here we examine its dynamical evolution in detail.

2.2. The physical problem

The specific problem examined herein is illustrated schematically in figure 1. We consider homogeneous shear of a viscoelastic fluid with shear rate $\dot{\gamma}$, onto which a weak, localized disturbance is superposed. Analysis of the same flow configuration has been instructive in Newtonian studies, for example as a prototypical flow for rapid distortion theory (Moffatt 1967; Townsend 1976). The same configuration was also used to examine the Orr amplification mechanism. For example, Farrell (1987) considered the evolution of a variety of linear disturbances to demonstrate the requirement of a net tilt of the disturbance streamlines against the mean shear for energy amplification to take place. In the context of wall-bounded turbulence, Jiménez (2013) used this base flow to investigate the role of linear growth mechanisms in bursting events.

For homogeneous shear the only non-zero entry of $\boldsymbol{\Gamma}$ is $\Gamma_{12} \equiv \dot{\gamma}$. The corresponding base-state conformation for an Oldroyd-B fluid is

$$\mathbf{C} = \begin{pmatrix} 1 + 2\dot{\gamma}^2 \zeta^2 & \dot{\gamma} \zeta & 0 \\ \dot{\gamma} \zeta & 1 & 0 \\ 0 & 0 & 1 \end{pmatrix}. \quad (2.12)$$

The expressions for C_{ij} in a FENE-P fluid are similar in form and are provided in appendix A.

For the perturbation field, a Gaussian vortex of characteristic size l is chosen as the initial condition,

$$\mathbf{u}(\mathbf{x}, t = 0) = \alpha(\mathbf{e}_z \wedge \mathbf{x}) \exp(-(x^2 + y^2)/l^2), \quad (2.13)$$

while the initial perturbation polymer stresses are set to zero. The quantity α provides a measure of the vortex rotation rate. The condition that the vortex is deformed by the shear much faster than it rolls over, $\dot{\gamma}/\alpha \gg 1$, ensures that the dynamics are accurately described by the linear perturbation equations. The axisymmetric initial condition also enables a useful comparison between the viscoelastic and Newtonian configurations. In the latter case, an axisymmetric disturbance with no net tilt against the shear will simply decay (see Farrell 1987, and also § 3.1). Any amplification in the polymeric flow can therefore be attributed to the influence of elasticity.

The present interest in two-dimensional disturbances motivates the introduction of the vector potentials,

$$\mathbf{u} = \nabla \wedge \boldsymbol{\Psi}, \quad (2.14a)$$

$$\mathbf{f} = \nabla \wedge \boldsymbol{\Phi}, \quad (2.14b)$$

where $\boldsymbol{\Psi} = (0, 0, \psi)$ and $\boldsymbol{\Phi} = (0, 0, \varphi)$. In this form the velocity is written in terms of the perturbation streamfunction, ψ , while φ will be referred to as the polymer potential. Lines of constant φ are instantaneously parallel to the polymer perturbation force vectors. Furthermore, we may adopt the scalar definitions for the vorticity and polymer torque: $\omega \equiv \boldsymbol{\omega} \cdot \mathbf{e}_z = -\nabla^2 \psi$, $\chi \equiv \boldsymbol{\chi} \cdot \mathbf{e}_z = -\nabla^2 \varphi$. According to (2.10) and (2.11), the spanwise vorticity and polymer torque satisfy

$$\frac{\partial \omega}{\partial t} + \dot{\gamma} y \frac{\partial \omega}{\partial x} = \frac{\beta}{R} \nabla^2 \omega + \frac{(1 - \beta)}{R} \chi, \quad (2.15a)$$

$$\frac{\partial \chi}{\partial t} + \dot{\gamma} y \frac{\partial \chi}{\partial x} + \frac{1}{W} \chi = 2\dot{\gamma} \frac{\partial^2 \varphi}{\partial x \partial y} + T_{jk} \frac{\partial^2 \omega}{\partial x_j \partial x_k} + \frac{1}{W} \nabla^2 \omega. \quad (2.15b)$$

Equation (2.15b) is non-dimensionalized by the shear rate, $\dot{\gamma}$, and the vortex size l . This choice yields the following definitions of the Reynolds and Weissenberg numbers:

$$R \equiv \frac{\dot{\gamma} l^2}{\nu}, \quad W \equiv \dot{\gamma} \zeta, \quad (2.16a,b)$$

while $\beta = \mu_s/\mu$ is the ratio of solvent to total viscosity. The unit dimensionless shear rate, $\dot{\gamma}$, will be retained in the equations for clarity.

An important term appearing in (2.15b) is $2\dot{\gamma} \partial_{xy}^2 \varphi \equiv \dot{\gamma}(\partial_x f_x - \partial_y f_y)$, which is the kinematic torque amplification mechanism mentioned in connection with (2.11) and which will be described in § 3. The term $T_{jk} \partial_{jk}^2 \omega$ in (2.15b) describes the generation of polymer torque due to the distortion of the mean polymer stresses by curvature in the vorticity field, and is analogous to the term involving velocity perturbations in the polymer force equation (2.8). For long relaxation times, or high Weissenberg numbers, it has a strongly anisotropic character due to the large streamwise base-state stresses.

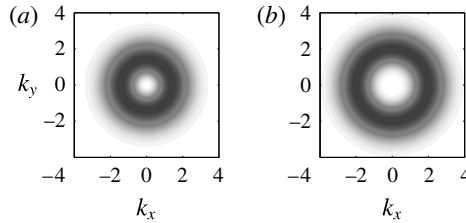


FIGURE 2. (a) The spectral energy, $|\hat{u}(\mathbf{k}, 0)|^2 + |\hat{v}(\mathbf{k}, 0)|^2$, and (b) enstrophy, $|\hat{w}(\mathbf{k}, 0)|^2$, densities in the initial vortex (2.13).

2.3. Fourier decomposition

Since the flow is homogeneous in both the streamwise and cross-stream directions, the two-dimensional Fourier transform is introduced:

$$\omega(\mathbf{x}, t) = \frac{1}{(2\pi)^2} \iint_{-\infty}^{\infty} \hat{\omega}(\mathbf{k}, t) e^{i\mathbf{k}(t) \cdot \mathbf{x}} d^2\mathbf{k}. \tag{2.17}$$

The time evolution of the wavevector is given according to

$$k_x = \text{const.}, \quad k_y(t) = k_y - k_x \dot{\gamma} t. \tag{2.18}$$

The streamwise spacing of phase fronts remains unchanged, but the cross-stream wavenumber is altered as the disturbance is reorientated by the shear (unless $k_x = 0$). To avoid confusion, the dependence of the cross-stream wavenumbers on time will always be explicitly stated, i.e. we will always write $k_y(t)$, while k_y will be reserved for the initial value $k_y \equiv k_y(t = 0)$.

In Fourier space, the equations for the spanwise vorticity and torque become

$$\frac{d\hat{\omega}}{dt} = -\frac{\beta|\mathbf{k}(t)|^2}{R}\hat{\omega} + \frac{(1-\beta)}{R}\hat{\chi}, \tag{2.19a}$$

$$\frac{d\hat{\chi}}{dt} + \frac{1}{W}\hat{\chi} = -\frac{2\dot{\gamma}k_x k_y(t)}{|\mathbf{k}(t)|^2}\hat{\chi} - T_{11}k_x^2\hat{\omega} - 2T_{12}k_x k_y(t)\hat{\omega} - \frac{|\mathbf{k}(t)|^2}{W}\hat{\omega}. \tag{2.19b}$$

The quantity $|\mathbf{k}(t)|^2 \equiv k_x^2 + k_y^2(t)$ is the square of the instantaneous total wavenumber. The initial conditions in Fourier space are $\hat{\omega}(t = 0) = \hat{\omega}(0)$ and $\hat{\chi}(t = 0) = 0$. The spectral energy, $|\hat{u}(\mathbf{k}, 0)|^2 + |\hat{v}(\mathbf{k}, 0)|^2$, and enstrophy, $|\hat{w}(\mathbf{k}, 0)|^2$, densities in the initial vortex (2.13) are shown in figure 2. At times it is instructive to combine the coupled system (2.19b) into a single second-order equation for the vorticity:

$$\begin{aligned} \frac{d^2\hat{\omega}}{dt^2} + \left(\frac{1}{W} + \frac{\beta|\mathbf{k}(t)|^2}{R} + \frac{2\dot{\gamma}k_x k_y(t)}{|\mathbf{k}(t)|^2} \right) \frac{d\hat{\omega}}{dt} \\ + \left(\frac{(1-\beta)T_{11}k_x^2}{R} + \frac{2(1-\beta)T_{12}k_x k_y(t)}{R} + \frac{|\mathbf{k}(t)|^2}{RW} \right) \hat{\omega} = 0. \end{aligned} \tag{2.20}$$

The initial condition on the time derivative of the vorticity is obtained from the initial condition on the torque, $\hat{\chi}(t = 0) = 0$, which implies $d\hat{\omega}/dt(t = 0) = -\beta|\mathbf{k}(0)|^2\hat{\omega}(0)/R$.

The vorticity and torque equations will be used throughout the analysis. These equations (2.19b), or equivalently (2.20), constitute a linear coupled system. A

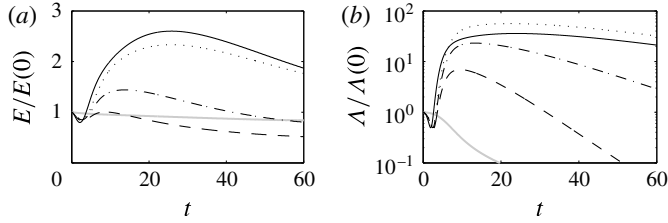


FIGURE 3. Example energy (a) and enstrophy (b) evolutions for the Gaussian vortex in an Oldroyd-B fluid: ----, $R = 200$, $W = 15$, $\beta = 0.8$; - · -, $R = 400$, $W = 30$, $\beta = 0.8$; —, $R = 400$, $W = 60$, $\beta = 0.8$; ·····, $R = 800$, $W = 60$, $\beta = 0.8$. The grey lines are the Newtonian case with $R = 800$.

general analytical solution is not known, and we will therefore analyse certain limiting cases of physical relevance. Complementary numerical results are presented, and are computed in Fourier space from the original linear system of equations in primitive variables; see appendix A for the equations and a description of the numerical solution technique.

3. Oldroyd-B fluids

Time evolutions of the energy and enstrophy,

$$E(t) = \iint \frac{\rho |\mathbf{u}|^2}{2} d^2\mathbf{x} \quad \text{and} \quad \Lambda(t) = \iint \frac{|\omega|^2}{2} d^2\mathbf{x}, \tag{3.1a,b}$$

of the Gaussian vortex in an Oldroyd-B fluid are reported in figure 3 for several parameters, alongside a Newtonian case computed at $R = 800$. In the Newtonian evolution the energy and enstrophy do not exhibit any amplification. The behaviour of the energy is anticipated based on the criterion for Orr amplification, since the streamlines of the vortex do not have net tilt against the mean shear (a summary of the inviscid Orr amplification is provided in §3.1). Instead, the energy simply decays due to the action of viscosity. The enstrophy is solely composed of spanwise vorticity and, in the present two-dimensional flow, there is no linear Newtonian mechanism for spanwise vorticity generation. As a result, the enstrophy also decays by the action of viscosity. The viscoelastic results are a striking departure from the Newtonian behaviour. Firstly, the energy amplifies, and secondly, there is a large enstrophy amplification at high Weissenberg numbers. Finally, note that both energy and enstrophy growth are preceded by an initial period of decay at early times for all the viscoelastic cases considered in figure 3.

Contours of the spanwise vorticity and the streamfunction are reported in figure 4 for one set of parameters from figure 3. The Reynolds number, $R = 400$, and Weissenberg number, $W = 60$, are both fairly large, and are representative of larger eddies in strong shear. There are two noteworthy features, both of which will be explored in detail in this section. (i) As the vortex tilts under the action of the mean shear it splits into a co-rotating pair. This behaviour coincides with the early dip in the energy and enstrophy reported in figure 3. (ii) Beyond $t = 3$, a patch of negative vorticity forms between the two detached regions of positive vorticity, which become extended in long stripes due to the action of the mean shear. As advection by the base flow continues to rotate and extend the disturbance, these stripes of vorticity begin

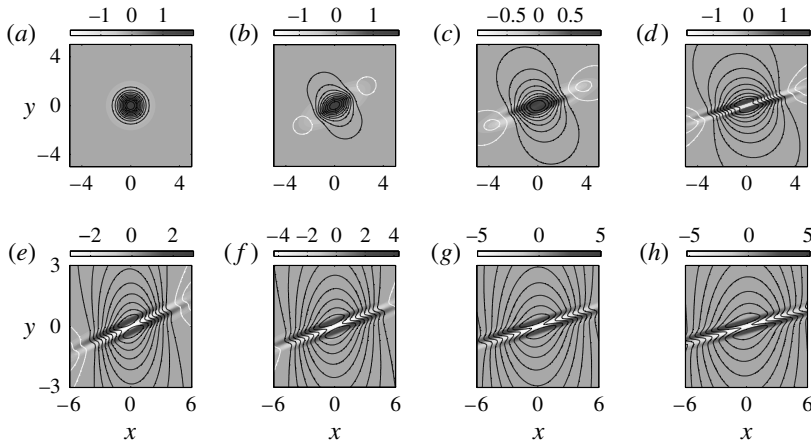


FIGURE 4. Time evolution of the vorticity (shading) and streamfunction (lines) for the Gaussian vortex in an Oldroyd-B fluid. Here, $R = 400$, $W = 60$ and $\beta = 0.8$. The instantaneous fields correspond to $t = \{0, 1, 2, \dots, 7\}$. Note the change in aspect ratio for $t \geq 4$.

to amplify. Neither of these features, namely the vortex splitting and the subsequent amplification of vorticity, is observed in a Newtonian fluid.

This section focuses on the mechanisms which lead to the phenomenology described above. First, a brief review of the Newtonian Orr amplification mechanism is provided in §3.1. In §3.2 the ability of a viscoelastic fluid to support the propagation of vorticity waves is introduced for the case of zero mean shear. The limit of high elasticity allows us to isolate the cause of the splitting of the vortex in §3.3. In §3.4 the more realistic case of small-to-moderate elasticity is examined, and the mechanism of vorticity growth is explained. The long-time decay of the vortex is addressed in §3.5. Finally, a physical discussion of the results is presented in §3.6.

3.1. The Orr mechanism in Newtonian fluids

A correct interpretation of the viscoelastic results benefits from an understanding of the Newtonian Orr mechanism. A brief review is presented here; a more detailed treatment can be found in the literature on Newtonian flows (e.g. Farrell 1987).

Consider the perturbation vorticity equation for an inviscid Newtonian fluid in spectral space,

$$\frac{d\hat{\omega}}{dt} = 0. \tag{3.2}$$

The solution, $\hat{\omega}(t) = \hat{\omega}(0)$, indicates that the perturbation vorticity is a purely advected quantity, and a localized disturbance constructed from a superposition of these plane-wave solutions retains this character. This result is intuitive since the two-dimensionality removes any stretching or tilting effects.

In terms of the streamfunction, $\hat{\psi} = \hat{\omega}/|\mathbf{k}(t)|^2$, and therefore (3.2) is equivalent to

$$\frac{d\hat{\psi}}{dt} = \frac{2\dot{\gamma}k_x k_y(t)}{|\mathbf{k}(t)|^2} \hat{\psi}. \tag{3.3}$$

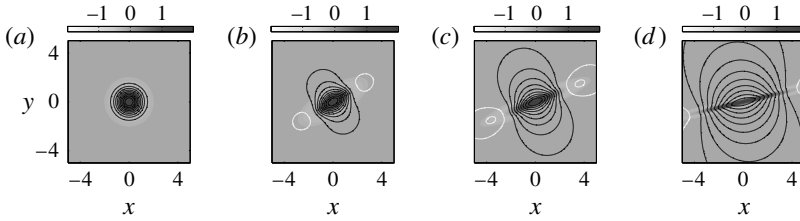


FIGURE 5. Evolution of the counter-rotating Gaussian vortex in an inviscid Newtonian flow. From left to right, $t = \{0, 1, 2, 4\}$. The perturbation energy is unchanged throughout the evolution, $E(t) = E(0) \forall t$.

The streamfunction can amplify in time and, by extension, so can the kinetic energy. The right-hand side of (3.3) can be traced back to the pressure-gradient terms in the momentum equations, and reflects the role of mass conservation in the amplification process. The disturbance amplifies in time if the product $k_x k_y(t) > 0$, which is true when the disturbance phase fronts are instantaneously aligned against the shear.

In physical space, a realistic localized disturbance is constructed from a set of plane waves according to (2.17). Consequently it may contain both growing and decaying modes, and the overall energy evolution is a superposition of the two behaviours (Farrell 1987). An initially symmetric disturbance, such as the Gaussian vortex considered here, samples all wavevector orientations equally for a given wavenumber magnitude. In this instance, there is no overall amplification or decay and the net effect of the term on the right-hand side of (3.3) is muted. This can also be clearly seen from the perturbation energy equation in physical space (Farrell 1987; Butler & Farrell 1992):

$$\begin{aligned}
 \frac{dE}{dt} &= - \iint \rho uv \dot{\gamma} d^2\mathbf{x}, \\
 &= \iint \rho \frac{\partial \psi / \partial x}{\partial \psi / \partial y} \left(\frac{\partial \psi}{\partial y} \right)^2 \dot{\gamma} d^2\mathbf{x}, \\
 &= - \iint \rho \left(\frac{\partial y}{\partial x} \right)_\psi \left(\frac{\partial \psi}{\partial y} \right)^2 \dot{\gamma} d^2\mathbf{x}.
 \end{aligned} \tag{3.4}$$

The Reynolds stress has been rewritten in terms of the slope of the streamlines $(\partial y / \partial x)_\psi$, and the equation has been integrated along a unit length in the span. Thus, the condition $k_x k_y(t) > 0$ for plane waves becomes a requirement for a net tilt in the streamlines of a localized disturbance against the shear.

Snapshots of the perturbation vorticity and streamfunction computed at four subsequent time instances in an inviscid Newtonian fluid are provided in figure 5. The disturbance is rotated and extended by the shear, but the total energy and enstrophy remain constant.

3.2. Zero mean-shear: the equations of linear viscoelasticity

The effects of viscoelasticity on the disturbance evolution are now reintroduced, but are first limited to the case of zero background shear. This particular limit serves to illustrate the mechanism by which viscoelastic fluids support the propagation of vorticity waves.

In the absence of mean shear, the vorticity–torque system (2.19*b*) simplifies to

$$\frac{d\hat{\omega}}{dt} = -\frac{\beta\kappa^2}{R}\hat{\omega} + \frac{(1-\beta)}{R}\hat{\chi}, \quad (3.5a)$$

$$\frac{d\hat{\chi}}{dt} + \frac{1}{W}\hat{\chi} = -\frac{\kappa^2}{W}\hat{\omega}, \quad (3.5b)$$

where $\kappa^2 \equiv |\mathbf{k}(0)|^2$ is constant since there is no reorientation of the wavevector with time. Note that when $\dot{\gamma} = 0$, the Reynolds and Weissenberg numbers must be redefined using a new time scale, here the vortex rotation rate, α^{-1} . Equations (3.5*a,b*) are those of linear viscoelasticity. On the right-hand side of (3.5*a*) are solvent diffusion and the polymer torque. The diffusion term can also be regarded as a viscous torque in the solvent. The behaviour of this system is most evident by combining (3.5*b*) into a second-order equation for the vorticity (cf. (2.20)):

$$\frac{d^2\hat{\omega}}{dt^2} + \left(\frac{1}{W} + \frac{\beta\kappa^2}{R}\right)\frac{d\hat{\omega}}{dt} - \frac{\kappa^2}{RW}\hat{\omega} = 0. \quad (3.6)$$

This is an equation for a damped harmonic oscillator. The damping is due to both relaxation and diffusion in the solvent. The two solutions to (3.6) have an exponential dependence, $\hat{\omega}(t) \sim \exp(-im^\pm t)$, where

$$m^\pm = -\frac{i}{2W} \left(\Theta + 1 \pm \sqrt{(1 + \Theta)^2 - \frac{4\Theta}{\beta}} \right). \quad (3.7)$$

The two roots depend on the parameter $\Theta \equiv W\beta\kappa^2/R = \zeta\nu_s\kappa^2$, which is the ratio of the relaxation time to the disturbance diffusion time scale in the solvent. The significance of this parameter was explained by Page & Zaki (2014) and is summarized here. For either the Newtonian, $\Theta \ll 1$, or the elastic case, $\Theta \gg 1$, the roots are imaginary and the associated solutions to (3.6) are purely decaying. When Θ is of the order of unity, the roots have a real component and correspond to propagating vorticity waves in physical space. The precise range of Θ for which propagation of vorticity waves is supported, i.e. $\text{Re}(m) \neq 0$, depends on β alone, and expands in the limit of a vanishing solvent (see (3.7)). For a fixed set of flow parameters, $\{R, W, \beta\}$, this range of $\Theta \equiv W\beta\kappa^2/R$ can be interpreted as a range of wavenumbers, κ . Therefore, when β is very small, the wide range of wavenumbers indicates that the evolution of the Gaussian vortex is dominated by wave propagation. An example of this behaviour is displayed in figure 6.

For dilute solutions, the criteria for wave propagation presented above are satisfied for only a small range of wavenumbers. This follows from the fact that the generation of polymer torque according to (3.5*b*) is due to the familiar viscous term $-\kappa^2\hat{\omega}$ and, for larger β , diffusion in the solvent ensures that most modes are purely decaying. However, in the presence of mean shear the forcing on the right-hand side of (3.5*b*) is augmented by a term $-k_j k_k T_{jk}\hat{\omega}$. The large streamwise stress T_{11} can potentially generate a large polymer torque. As a result, wave propagation may become important for a much broader range of wavenumbers, and this effect is now explored in the context of vortex splitting.

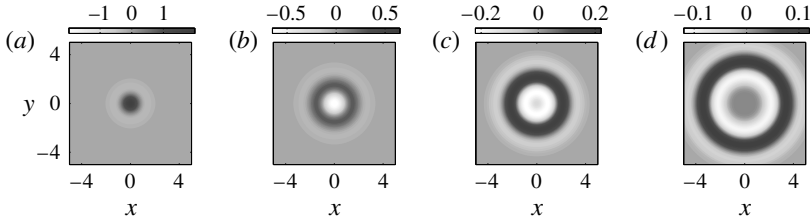


FIGURE 6. Contours of spanwise vorticity for $\dot{\gamma} = 0$. Here $\Theta_l \equiv W\beta\kappa^2/R = 0.95$, with $W = 50$, $R = 5$, $\beta = 0.1$. Snapshots correspond to $t = \{0, 10, 20, 30\}$.

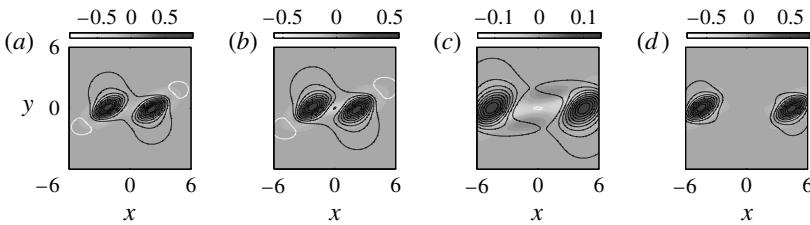


FIGURE 7. Spanwise vorticity (shading) and streamfunction (lines) at $t = 1$: (a,b) $E^* \equiv W(1 - \beta)/R = 2.5$, with $R = 10$, $\beta = 0.5$, $W = 50$ and $R = 5$, $\beta = 0.8$, $W = 62.5$ respectively; (c,d) $E = 10$, with $R = 1$, $\beta = 0.8$, $W = 50$ and $R = 5$, $\beta = 0.5$, $W = 100$ respectively.

3.3. Vortex splitting

We now return to the full problem with a finite shear rate. The splitting of the Gaussian vortex observed in figure 4 can be isolated from the subsequent amplification by considering the limit of high elasticity, $E^* \equiv W(1 - \beta)/R$. Figure 7 shows snapshots at $t = 1$ from calculations of vortex evolutions for four sets of flow parameters, $\{R, W, \beta\}$, which correspond to two values of E^* . Panels (a,b) are at $E^* = 2.5$, and (c,d) are at $E^* = 10$. The original vortex separates into a pair of new vortices which propagate in x , while their cores remain approximately aligned. While the vortex evolution, for example the vorticity magnitude, depends on all flow parameters, the streamwise location of the vortex cores at $t = 1$ is unchanging for fixed values of E^* . Also, the vortex splitting is more rapid for the relatively large values of E^* .

The evolution of enstrophy is reported in figure 8(a). In all four cases there is a period of rapid decay in Λ for $t \lesssim 0.5$ associated with the splitting of the Gaussian vortex into the new pair of vortices. Subsequently, there is a small increase in Λ in all but the lowest Reynolds number case, after which the enstrophy is monotonically decaying with time. Streamwise enstrophy spectra are reported in figure 8(b). For a given wavenumber, k_x , the enstrophy is oscillatory in time, and there is a continuous phase difference in the oscillations across wavenumbers. This trend is indicative of the mechanism of vorticity-wave propagation in physical space, which was discussed in § 3.2 in the absence of background mean shear. However, the oscillations do not persist for all streamwise wavenumbers, notably becoming muted as $k_x \rightarrow 0$. Global decay also sets in quickly for the smaller Reynolds numbers considered in figure 8, $R = \{1, 5\}$, where dissipation of enstrophy in the solvent is more pronounced.

In the subsequent analysis, we extract anisotropic vorticity wave propagation from the equations for the spanwise vorticity and polymer torque (2.19b) by adopting the assumption of high Weissenberg number. In this limit the relaxation of the polymer

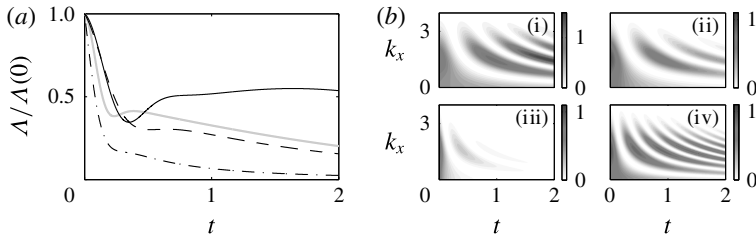


FIGURE 8. (a) Enstrophy evolutions for the Gaussian vortex: —, $R = 10$, $\beta = 0.5$, $W = 50$, with $E^* = 2.5$; ----, $R = 5$, $\beta = 0.8$, $W = 62.5$, with $E^* = 2.5$; — · —, $R = 1$, $\beta = 0.8$, $W = 50$, with $E^* = 10$; grey line, $R = 5$, $\beta = 0.5$, $W = 100$, with $E^* = 10$. (b) Streamwise enstrophy spectra. The labels (i)–(iv) correspond to the four parameter sets listed for (a).

may be neglected on the time scale of the background shear, $\dot{\gamma}^{-1}$, and the only relevant base-state stress is T_{11} . The further assumption of high elasticity allows us to derive a dispersion relation for the vorticity wave which describes the oscillation reported in figure 8. These vorticity waves travel much faster than the rate at which fluid elements are deformed by the shear. This separation of time scales motivates a multiple-scales analysis which demonstrates that the mean shear modulates the evolution of the vorticity waves.

Under the assumption of high Weissenberg number, the following expansions for the spanwise vorticity and polymer torque are adopted:

$$\hat{\omega}(t) = \hat{\omega}_0(t) + W^{-1}\hat{\omega}_1(t) + \dots, \tag{3.8a}$$

$$\hat{\chi}(t) = W\hat{\chi}_0(t) + \hat{\chi}_1(t) + \dots. \tag{3.8b}$$

Substitution into (2.19b) yields

$$\frac{d\hat{\omega}_0}{dt} = -\frac{\beta|\mathbf{k}(t)|^2}{R}\hat{\omega}_0 + E^*\hat{\chi}_0, \tag{3.9a}$$

$$\frac{d\hat{\chi}_0}{dt} = -\frac{2\dot{\gamma}k_xk_y(t)}{|\mathbf{k}(t)|^2}\hat{\chi}_0 - \frac{T_{11}}{W}k_x^2\hat{\omega}_0. \tag{3.9b}$$

Note that $T_{11} \equiv 2W\dot{\gamma}^2$. In this derivation we have assumed that $k_x, k_y(t) = O(1)$. The leading-order approximation (3.9b) remains valid over a time interval $t \lesssim O(W)$. Beyond this time horizon, reorientation of the disturbance by the shear increases the wall-normal wavenumber and $k_y(t \sim W) \neq O(1)$.

The system (3.9b) may be combined into a single vorticity equation (cf. (2.20)):

$$\frac{d^2\hat{\omega}_0}{dt^2} + \left(\frac{\beta|\mathbf{k}(t)|^2}{R} + \frac{2\dot{\gamma}k_xk_y(t)}{|\mathbf{k}(t)|^2} \right) \frac{d\hat{\omega}_0}{dt} + k_x^2\mathcal{B}\hat{\omega}_0 = 0. \tag{3.10}$$

We have introduced the definition $\mathcal{B} \equiv (1 - \beta)T_{11}/R$ in the spring constant. Note that \mathcal{B} is related to E^* , the elasticity parameter, by $\mathcal{B} = 2E^*\dot{\gamma}^2$. It was remarked in connection with figure 7 that the speed of propagation of the vortices depends on E^* . In (3.10), the spring constant, or natural frequency of oscillation, retains this dependence. Rescaling time by the natural frequency of oscillation, $\tau = k_x\sqrt{\mathcal{B}}t$, and setting $\bar{\omega}_0(\tau) = \hat{\omega}_0(t)$, (3.10) becomes

$$\frac{d^2\bar{\omega}_0}{d\tau^2} + \frac{1}{k_x\sqrt{\mathcal{B}}} \left(\frac{\beta|\mathbf{k}(\tau)|^2}{R} + \frac{2\dot{\gamma}k_xk_y(\tau)}{|\mathbf{k}(\tau)|^2} \right) \frac{d\bar{\omega}_0}{d\tau} + \bar{\omega}_0 = 0, \tag{3.11}$$

where $k_y(\tau) = k_y - \dot{\gamma}\tau/\sqrt{\mathcal{B}}$.

In the high-elasticity limit, $k_x\sqrt{\mathcal{B}} \gg 1$, the damping term in (3.11) becomes insignificant on the time scale set by the oscillation. The wavevector is also slowly changing over these short time intervals, $k_y(\tau) \approx \text{const}$. This scale separation motivates the use of the method of multiple scales (Bender & Orszag 1978), where the slow time scale based on the inverse shear rate, t , is reintroduced as an independent variable alongside the fast time, τ . The leading-order vorticity, $\bar{\omega}_0(\tau)$, is then written as an asymptotic series,

$$\bar{\omega}_0(\tau) = \bar{\omega}_0^0(\tau, t) + \varepsilon\bar{\omega}_0^1(\tau, t) + \dots, \quad (3.12)$$

where $\varepsilon \equiv 1/k_x\sqrt{\mathcal{B}} \ll 1$. The derivatives are also rewritten:

$$\frac{d}{d\tau} = \frac{\partial}{\partial\tau} + \varepsilon \frac{\partial}{\partial t}, \quad \frac{d^2}{d\tau^2} = \frac{\partial^2}{\partial\tau^2} + 2\varepsilon \frac{\partial^2}{\partial\tau\partial t} + \varepsilon^2 \frac{\partial^2}{\partial t^2}. \quad (3.13a,b)$$

Under this transformation and assuming the expansion (3.12), the leading-order and first-order corrections are found to evolve according to

$$\frac{\partial^2 \bar{\omega}_0^0}{\partial\tau^2} + \bar{\omega}_0^0 = 0, \quad (3.14a)$$

$$\frac{\partial^2 \bar{\omega}_0^1}{\partial\tau^2} + \bar{\omega}_0^1 = -2 \frac{\partial^2 \bar{\omega}_0^0}{\partial\tau\partial t} - \left(\frac{\beta|\mathbf{k}(t)|^2}{R} + \frac{2\dot{\gamma}k_x k_y(t)}{|\mathbf{k}(t)|^2} \right) \frac{\partial \bar{\omega}_0^0}{\partial\tau}. \quad (3.14b)$$

At leading order the initial conditions are simplified, $\bar{\omega}_0^0(\tau = 0) = \hat{\omega}(0)$, $\partial_\tau \bar{\omega}_0^0(\tau = 0) = 0$.

The solution of the leading-order equation (3.14a),

$$\bar{\omega}_0^0(\tau, t) = A(t) \cos(\tau + \theta(t)), \quad (3.15)$$

is purely oscillatory on the fast time scale, $\tau \equiv k_x\sqrt{\mathcal{B}}t$. In physical space this solution corresponds to left and right streamwise travelling waves of vorticity along the tensioned streamlines at speed $\sqrt{\mathcal{B}}$.

Contours of the spanwise vorticity and polymer torque for a vortex evolution with high elasticity, $E^* = 10$, are provided in figure 9. These snapshots were obtained from numerical solution of the full equations in primitive variables, and highlight the manner in which the propagation of the vorticity waves is confined to the streamwise direction. The propagation mechanism is similar to that described in §3.2. Polymer torque is generated due to the curvature in the vorticity perturbation acting on the mean polymer stress, $-T_{11}k_x^2\hat{\omega}$, on the right-hand side of (3.9b). In contrast to the zero-shear case, this term depends on streamwise curvature only: the large base-state stress, T_{11} , acts as a streamwise extensional viscosity. This is verified in figure 9 where the polymer torque at early times is proportional to the streamwise curvature of the vorticity field.

The effects of the damping term in (3.11), which includes solvent diffusion, can only be neglected on the time scale of the oscillation. For longer times damping is important, and is included in the multiple-scales solution at leading order through the slowly varying amplitude, $A(t)$, and phase, $\theta(t)$, of the oscillation in (3.15). Expressions for these functions are derived by requiring that the right-hand side of

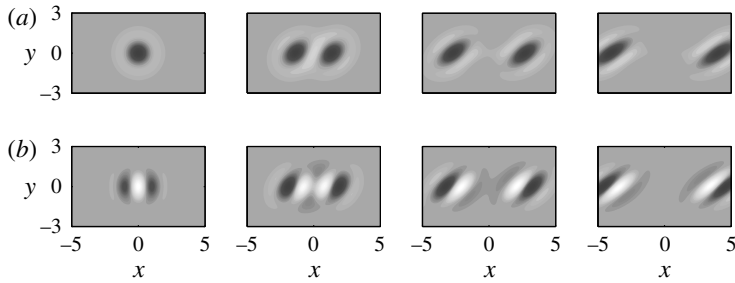


FIGURE 9. Contours of (a) spanwise vorticity and (b) polymer torque perturbations. In this example $W = 100$, $R = 5$, $\beta = 0.5$. Panes are extracted at $t = \{0^+, 0.3, 0.6, 0.9\}$.

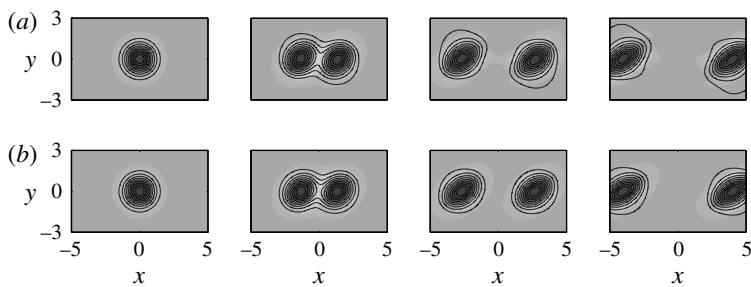


FIGURE 10. Contours of spanwise vorticity (shading) and streamfunction (lines) comparing the multiple-scales approximation (b) with the full numerical solution (a) at $W = 100$, $R = 5$, $\beta = 0.5$. Panes are extracted at $t = \{0^+, 0.3, 0.6, 0.9\}$.

the first-order correction (3.14b) does not include terms that lead to secular growth at $O(\varepsilon)$. This requirement is satisfied if

$$2 \frac{\partial^2 \bar{\omega}_0^0}{\partial \tau \partial t} + \left(\frac{\beta |\mathbf{k}(t)|^2}{R} + \frac{2\dot{\gamma} k_x k_y(t)}{|\mathbf{k}(t)|^2} \right) \frac{\partial \bar{\omega}_0^0}{\partial \tau} = 0, \tag{3.16}$$

from which we find $\theta(t) = 0$ and

$$A(t) = \underbrace{\hat{\omega}(0)}_{\left(\frac{|\mathbf{k}(t)|^2}{|\mathbf{k}(0)|^2} \right)^{1/2}} \exp \left(-\frac{\beta}{2R} \int^t |\mathbf{k}(t')|^2 dt' \right). \tag{3.17}$$

In figure 10 the leading-order multiple-scales approximation is compared with the solution of the full equation. The good agreement indicates that the approximation provides an accurate description of the dynamics across a range of wavenumbers. Note that the expression (3.17) for the envelope $A(t)$ also includes an algebraically growing component, which is identified by an underbrace. This growth is insignificant in the high elasticity limit, where the dynamics are dominated by fast oscillations and where decay is ensured by solvent diffusion. However, for low elasticities the growth is significant, and its origins are explained in detail in § 3.4.

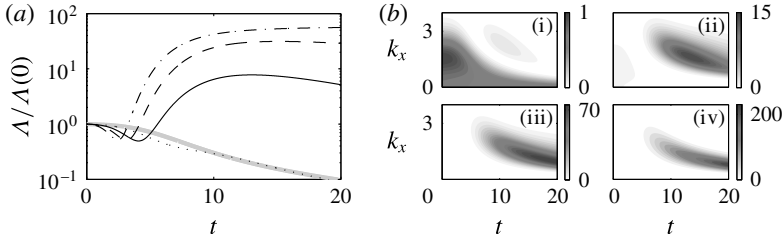


FIGURE 11. (a) Enstrophy evolutions with fixed $R = 800$, $\beta = 0.8$: \cdots , $W = 5$; $—$, $W = 15$; $- - -$, $W = 30$; $- \cdot -$, $W = 60$. The thick grey line is the Newtonian result at the same total Reynolds number. (b) Streamwise enstrophy spectra. The labels (i)–(iv) correspond to the four parameter sets listed for (a).

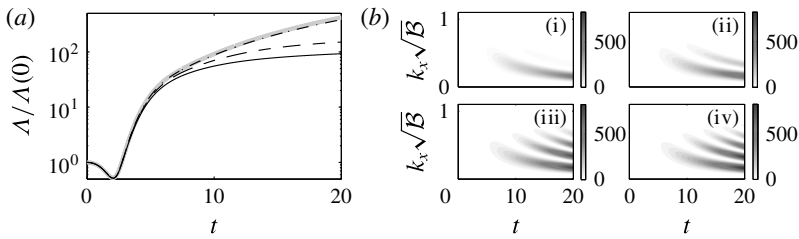


FIGURE 12. (a) Enstrophy evolutions with fixed $\mathcal{B} = 0.05$: $—$, $R = 1200$, $W = 100$, $\beta = 0.7$; $- - -$, $R = 2000$, $W = 100$, $\beta = 0.5$; $- \cdot -$, $R = 4000$, $W = 100$, $\beta = 0$. The grey line is the high Weissenberg number, high Reynolds number approximation (3.20). (b) Streamwise enstrophy spectra. The labels (i)–(iv) correspond to the four parameter sets listed for (a).

3.4. Spanwise vorticity amplification: a reverse-Orr mechanism

A selection of enstrophy evolutions for the Gaussian vortex are presented in figure 11(a) for much larger values of the Reynolds number, or lower elasticities, than those considered in § 3.3. The solvent Reynolds number is fixed and the Weissenberg number is varied. For low Weissenberg number ($W = 5$) the enstrophy is purely decaying, and deviation from the Newtonian curve is insignificant. This result is intuitive since the fast relaxation of the polymer chains means that the elastic component of the fluid simply behaves like an additional solvent. As the Weissenberg number is increased, significant enstrophy amplification is achieved. Streamwise enstrophy spectra are provided in figure 11(b). The amplification at high Weissenberg numbers is restricted to a narrow band of streamwise wavenumbers.

Further enstrophy evolutions are provided in figure 12(a). In this instance, the Weissenberg number is fixed at $W = 100$, and both R and β are varied such that the elastic wavespeed introduced in § 3.3, $\sqrt{\mathcal{B}}$, is constant. The curves collapse at short times, although decay sets in faster for lower solvent Reynolds numbers, R/β . Corresponding streamwise enstrophy spectra are presented in figure 12(b). In addition to the amplification, oscillations are also visible across a range of k_x for lower values of β , indicative of the wave propagation discussed in § 3.3. Note that the wavenumbers have been scaled by the vorticity wave speed, $\sqrt{\mathcal{B}}$. Under this normalization, it is clear that growth is most significant in modes with low frequencies, $k_x\sqrt{\mathcal{B}} < 1$.

The vorticity amplification mechanism is examined here in detail, again in the limit of high Weissenberg number. First, the physical origins of the vorticity growth are explained qualitatively. Matched asymptotic expansions are then employed to examine the evolution of low-frequency waves. The analysis establishes the dependence of the amplification on both the frequency, $k_x\sqrt{B}$, and the initial orientation of the wavevector, (k_x, k_y) . The connection between these results and the splitting behaviour examined in § 3.3 is reviewed in § 3.6.

Consider again the leading-order equations in the high Weissenberg number approximation (3.9b):

$$\frac{d\hat{\omega}_0}{dt} = -\frac{\beta|\mathbf{k}(t)|^2}{R}\hat{\omega}_0 + E^*\hat{\chi}_0, \tag{3.18a}$$

$$\frac{d\hat{\chi}_0}{dt} = \underbrace{-\frac{2\dot{\gamma}k_xk_y(t)}{|\mathbf{k}(t)|^2}}_{\mathcal{S}}\hat{\chi}_0 - \frac{T_{11}}{W}k_x^2\hat{\omega}_0. \tag{3.18b}$$

In the high-elasticity limit (§ 3.3), attention was focused on vortex splitting, and the term labelled \mathcal{S} had only a weak influence on the dynamics, causing a small modulation of the oscillation envelope. However, for the moderate elasticities considered here, or equivalently slower vorticity wave speeds, the effects of this term are dominant. There is an analogy between the amplification of polymer torque driven by $\mathcal{S}\hat{\chi}_0$ and the Orr mechanism for energy amplification in Newtonian fluids which was reviewed in § 3.1. This analogy is evident when $\mathcal{S}\hat{\chi}_0$ is compared to the term that causes Orr amplification on the right-hand side of (3.3). The Newtonian term is positive and the streamfunction amplifies when the wavefronts are instantaneously aligned against the shear. In contrast, here the term $\mathcal{S}\hat{\chi}_0$ has the opposite behaviour: perturbations with wavefronts aligned with the shear can experience an amplification in their polymer torque. This observation is significant because all perturbations, bar those with $k_x=0$, align with the shear as time increases.

It is by virtue of the solenoidal nature of the polymer force field that $\mathcal{S}\hat{\chi}_0$ has been written in the form appearing in (3.9b). While this presentation highlights the importance of the wavevector’s alignment relative to the shear, it masks the physical mechanism. The torque amplification is a kinematic effect which can be seen most clearly when $\mathcal{S}\hat{\chi}$ is expressed in its original form in terms of forces,

$$\mathcal{S}\hat{\chi} = \dot{\gamma}(ik_x\hat{f}_x - ik_y(t)\hat{f}_y). \tag{3.19}$$

The two terms on the right-hand side have a simple physical interpretation. A schematic illustrating the effects of each term in physical space is provided in figure 13. The first term, $\dot{\gamma}ik_x\hat{f}_x$, describes the change in torque induced at a point by the relative advection of layers of streamwise varying polymer force. The second term, $-\dot{\gamma}ik_y(t)\hat{f}_y$, is similar in character, but in this instance the streamwise force is first generated via the polymer stretch mechanism, whereby the shear causes a reorientation, or tilting, of the wall-normal polymer force which generates a streamwise force. The wall-normal variation of the force field results in a torque.

For a more detailed analysis of the torque amplification mechanism on spanwise vorticity growth, we consider the second-order vorticity equation in the limit of high Weissenberg number (3.10). However, since attention is focused on high Reynolds

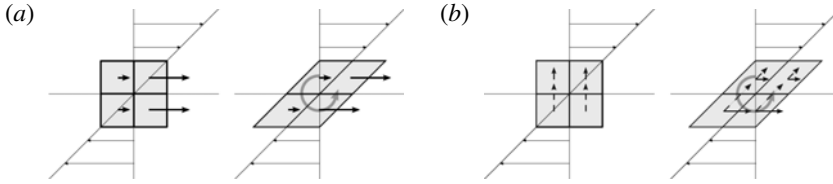


FIGURE 13. A schematic of the torque amplification mechanism. (a) A small element with $\partial_y f_x > 0$ is distorted by the mean shear to generate a local polymer torque. (b) A small element with $\partial_y f_y < 0$ is distorted to generate a streamwise force via the polymer stretch mechanism. The y -variation corresponds to a torque.

numbers, solvent diffusion is neglected in order to simplify the analysis:

$$\frac{d^2 \hat{\omega}_0}{dt^2} + \underbrace{\frac{2\dot{\gamma}(k_r - \dot{\gamma}t)}{1 + (k_r - \dot{\gamma}t)^2}}_{-\mathcal{S}} \frac{d\hat{\omega}_0}{dt} + k_x^2 \mathcal{B} \hat{\omega}_0 = 0. \quad (3.20)$$

In this equation the definition $k_r \equiv k_y/k_x = O(1)$ has been introduced for the initial gradient of the wavevector. The torque amplification mechanism, $\mathcal{S} \hat{\chi}_0$, appears in this oscillator equation as the damping term. The term becomes negative, which corresponds to an injection of vorticity, when the phase fronts are aligned with the shear. Our interest is the strongly amplifying, low-frequency modes, and hence we adopt the definition $\varepsilon \equiv k_x^2 \mathcal{B} \ll 1$.

Before proceeding, the validity of neglecting the solvent diffusion term in (3.20) should be assessed. The approximation (3.20) becomes exact in the special limit $W \rightarrow \infty$, $R \rightarrow \infty$, with W/R finite. In this sense it is equivalent to the elastic Rayleigh equation (Azaiez & Homsy 1994; Rallison & Hinch 1995; Ray & Zaki 2014, 2015), which has been used to examine the stability of viscoelastic free-shear flows. In the present problem the role of solvent diffusion is to act as a damper with a time-dependent strength. This damping becomes increasingly effective as the disturbance aligns with the shear and the sharpening gradients increase the rate of momentum diffusion. As such, the approximation (3.20) becomes increasingly inaccurate at capturing the enstrophy evolution as time advances, and this effect is seen in the results reported in figure 12(a). For lower solvent Reynolds numbers, R/β , the exact enstrophy evolution deviates quickly from that predicted by (3.20). The streamwise enstrophy spectra presented in figure 12(b) reveal that solvent diffusion tends to damp high-frequency oscillations, which persist in the solution to (3.20). However, the most significant enstrophy amplification is associated with low-frequency modes, $k_x \sqrt{\mathcal{B}} < 1$, which is present in the solutions to both the full equations with finite β , and the approximation (3.20).

It is instructive to analyse (3.20) further using matched asymptotic expansions, since the equation provides an upper bound on the amplification at early times and its dynamics provide an uncluttered view of the amplification mechanism. With the removal of solvent diffusion and once the disturbance aligns with the shear, $k_y(t)/k_x < 0$, there are no sinks of vorticity in (3.20) and, as a result, the disturbance continues to amplify as $t \rightarrow \infty$. In reality, vorticity decays at long time due to the action of solvent diffusion and other terms that were neglected in the high Weissenberg number approximation (3.9b). These effects will be examined in § 3.5.

Inner solution

The vorticity is expanded as an asymptotic series in powers of ε , $\hat{\omega}_0(t) = \hat{\omega}_0^0(t) + \varepsilon \hat{\omega}_0^1(t) + \dots$. Substituting into (3.20), the leading-order and first-order equations are

$$\left(\frac{d}{dt} + \frac{2\dot{\gamma}(k_r - \dot{\gamma}t)}{1 + (k_r - \dot{\gamma}t)^2} \right) \frac{d\hat{\omega}_0^0}{dt} = 0, \tag{3.21a}$$

$$\underbrace{\left(\frac{d}{dt} + \frac{2\dot{\gamma}(k_r - \dot{\gamma}t)}{1 + (k_r - \dot{\gamma}t)^2} \right)}_{-\mathcal{L}} \frac{d\hat{\omega}_0^1}{dt} = -\hat{\omega}_0^0. \tag{3.21b}$$

In the absence of solvent diffusion, the polymer torque is related to the vorticity gradient by $\hat{\chi}_0(t) = R(1 - \beta)^{-1} d\hat{\omega}_0/dt$. Therefore it is helpful to think of the first-order equation (3.21b) as a forced equation for the polymer torque, or a one-way coupling from the flow perturbation to the polymer. Without the solvent, the initial conditions are simplified: at leading order we apply $\hat{\omega}_0^0(t=0) = \hat{\omega}(0)$ and $d_t \hat{\omega}_0^0(t=0) = 0$; higher-order corrections have homogeneous initial conditions.

The solution to (3.21b) gives an expression for $\hat{\omega}_0(t)$ up to $O(\varepsilon)$:

$$\hat{\omega}_0(t) = \hat{\omega}(0) \left(1 + \frac{\varepsilon}{\dot{\gamma}^2} \left[\frac{(k_r - \dot{\gamma}t)^2 - k_r^2}{6} + \frac{1}{3} \log \left(\frac{1 + (k_r - \dot{\gamma}t)^2}{1 + k_r^2} \right) - (k_r - \dot{\gamma}t) \left(1 + \frac{(k_r - \dot{\gamma}t)^2}{3} \right) (\tan^{-1}(k_r - \dot{\gamma}t) - \tan^{-1} k_r) \right] \right). \tag{3.22}$$

The vorticity is constant to leading order on account of the absence of an initial torque. Amplification is possible at first order, however. The growth at first order in (3.22) violates the adopted asymptotic series when $t \sim O(\varepsilon^{-1/3})$, and again later at $t \sim O(\varepsilon^{-1/2})$. More precisely, the series expansion becomes invalid when the wavenumber ratio $k_y(t)/k_x \equiv (k_r - \dot{\gamma}t) = O(\varepsilon^{-1/3})$. Therefore, we define the shifted time $\xi = (k_r - \dot{\gamma}t)/\dot{\gamma}$ as our new independent variable. Note that ξ is essentially a scaled cross-stream wavenumber, and becomes negative when the phase fronts are aligned with the shear. In the large- ξ limit (3.22) becomes

$$\hat{\omega}_0(\xi) \sim \hat{\omega}(0) \left(1 + \varepsilon \left[\left(\frac{\pi}{2} + \tan^{-1} k_r \right) \frac{\dot{\gamma} \xi^3}{3} + \frac{\xi^2}{2} + \dots \right] \right). \tag{3.23}$$

Intermediate solution

In order to extend the validity of the asymptotic solution beyond $\xi = O(\varepsilon^{-1/3})$, an intermediate variable is defined, $\eta \equiv \xi \varepsilon^{1/3}$, with which the governing equation (3.20) becomes

$$\varepsilon^{2/3} \frac{d^2 \tilde{\omega}_0}{d\eta^2} - \frac{2\dot{\gamma}^2 \eta}{1 + \dot{\gamma}^2 \eta^2 \varepsilon^{-2/3}} \frac{d\tilde{\omega}_0}{d\eta} + \varepsilon \tilde{\omega}_0 = 0, \tag{3.24}$$

where $\tilde{\omega}_0(\eta) = \hat{\omega}_0(\xi)$. The large- ξ limit of the inner solution (3.23) suggests an intermediate expansion $\tilde{\omega}_0(\eta) = \tilde{\omega}_0^0(\eta) + \varepsilon^{1/3} \tilde{\omega}_0^1(\eta) + \dots$. The leading-order and first-order corrections satisfy

$$\left(\frac{d}{d\eta} - \frac{2}{\eta}\right) \frac{d\tilde{\omega}_0^0}{d\eta} = 0, \tag{3.25a}$$

$$\left(\frac{d}{d\eta} - \frac{2}{\eta}\right) \frac{d\tilde{\omega}_0^1}{d\eta} = -\tilde{\omega}_0^0. \tag{3.25b}$$

The solution correct to $O(\varepsilon^{1/3})$ reads

$$\tilde{\omega}_0(\eta) = \tilde{A}_{01} \frac{\eta^3}{3} + \tilde{A}_{02} + \varepsilon^{1/3} \left[\tilde{A}_{11} \frac{\eta^3}{3} + \tilde{A}_{12} + \left(\tilde{A}_{02} \frac{\eta^2}{2} - \tilde{A}_{01} \frac{\eta^5}{30} \right) \right]. \tag{3.26}$$

The constants can be evaluated from matching with the inner solution. By writing (3.23) as a function of the intermediate variable, $\hat{\omega}_0(\eta)$, and comparing terms with (3.26), we find $\tilde{A}_{11} = \tilde{A}_{12} = 0$ and

$$\tilde{A}_{01} = \hat{\omega}(0) \dot{\gamma} \left(\frac{\pi}{2} + \tan^{-1} k_r \right), \quad \tilde{A}_{02} = \hat{\omega}(0). \tag{3.27a,b}$$

Outer solution

The intermediate solution (3.26) breaks down when $\eta = O(\varepsilon^{-1/6})$, or when $\xi = O(\varepsilon^{-1/2})$. Therefore, we rewrite (3.20) in terms of the outer variable, $K \equiv \eta \varepsilon^{1/6} = \xi \varepsilon^{1/2}$,

$$\frac{d^2 \bar{\omega}_0}{dK^2} - \frac{2\dot{\gamma}^2 K}{\varepsilon + \dot{\gamma}^2 K^2} \frac{d\bar{\omega}_0}{dK} + \bar{\omega}_0 = 0, \tag{3.28}$$

where $\bar{\omega}_0(K) = \tilde{\omega}_0(\eta)$. The form of the intermediate solution (3.26) suggests an outer expansion, $\bar{\omega}_0(K) = \varepsilon^{-1/2} \bar{\omega}_0^{-1}(K) + \bar{\omega}_0^0(K) + \dots$. Notice that the leading term is $O(\varepsilon^{-1/2}) \equiv O(1/k_x \sqrt{B})$, which means the vorticity has been amplified by a factor inversely proportional to its frequency of oscillation. Both the leading-order and first-order terms satisfy the homogeneous equation

$$\frac{d^2 \bar{\omega}_0^j}{dK^2} - \frac{2}{K} \frac{d\bar{\omega}_0^j}{dK} + \bar{\omega}_0^j = 0. \tag{3.29}$$

The solution is

$$\bar{\omega}_0^j(K) = \bar{D}_{j1}(K \cos K - \sin K) + \bar{D}_{j2}(K \sin K + \cos K). \tag{3.30}$$

Expanding the trigonometric functions in the small- K limit and comparing terms with (3.26), we find

$$\bar{D}_{-11} = -\hat{\omega}(0) \dot{\gamma} \left(\frac{\pi}{2} + \tan^{-1} k_r \right), \quad \bar{D}_{-12} = 0, \tag{3.31a,b}$$

and

$$\bar{D}_{01} = 0, \quad \bar{D}_{02} = \hat{\omega}(0). \tag{3.32a,b}$$

In summary, the asymptotic solution has a triple-deck structure, and is given by (3.22) for $|\xi| \lesssim \varepsilon^{-1/3}$, (3.26) for $\varepsilon^{-1/3} \lesssim |\xi| \lesssim \varepsilon^{-1/2}$, and (3.30) for $|\xi| \gtrsim \varepsilon^{-1/2}$. In figure 14 the matched asymptotic expansions are compared to numerical solution of

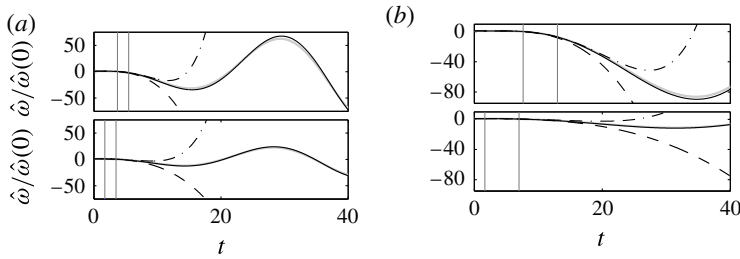


FIGURE 14. Comparison of the matched asymptotic expansions with numerical solution of (3.20): ----, inner solution; — · —, intermediate; —, outer. The numerical solution is shown in grey. (a) The two panels have $\varepsilon = 0.05$, with $k_r = 1$ and $k_r = -1$ respectively. (b) The two panels were computed with $\varepsilon = 0.01$, with $k_r = 3$ and $k_r = -3$ respectively. The vertical lines identify the points where $\xi = -\varepsilon^{-1/3}$ and $\xi = -\varepsilon^{-1/2}$. For a given ε the evolutions for $\pm k_r$ are plotted on the same scale to highlight the enhanced amplification for waves with an initial tilt against the shear, $k_r > 0$.

(3.20) for two values of $k_x\sqrt{B} \equiv \varepsilon^{1/2}$, each for a pair of initial orientations, $\pm k_r$. In both cases, good agreement is achieved throughout the time evolution.

The form of the outer solution (3.30) is interesting: it describes algebraically growing oscillations of frequency $k_x\sqrt{B}$. These oscillations correspond to streamwise propagating waves of vorticity in physical space, similar to the situation in § 3.3. Whilst all waves are amplifying once they are tilted with the shear, such that $|\xi| \gtrsim \varepsilon^{-1/2}$, the amplification rate of a particular mode exhibits a curious dependence on the initial gradient of the wavevector. This dependence is contained in the coefficient \bar{D}_{-11} , which can be written as $\bar{D}_{-11} = -\hat{\omega}(0)\dot{\gamma}(\phi + \pi/2)$. In this definition ϕ is the angle that the initial wavevector makes with the horizontal axis. If $k_x > 0$, for example, ϕ increases anticlockwise, and can take values $\phi \in [-\pi/2, \pi/2]$. For modes with a strong initial tilt with the shear, $\phi \rightarrow -\pi/2$, the amplification rate is comparatively weak. Conversely, for modes initially aligned against the shear, $\phi \rightarrow \pi/2$, the subsequent growth rate of the oscillations is large. This dependence of the amplitude of oscillation on the initial wavevector gradient is exhibited in the solutions presented in figure 14, where the evolutions of pairs of modes with equal and opposite ϕ are computed.

The preferential amplification of waves with an initial tilt against the shear is due to the fact that these modes reside for a longer duration in the ‘inner region’. The coefficient of ξ^3 in the inner-solution first-order correction (3.23) ultimately sets the value of \bar{D}_{-11} . It was remarked that the first-order correction, (3.21b), can be considered as a forced equation for the polymer torque. The inner region also contains the range of wavevector orientations for which \mathcal{S} has its maximum. The longer a mode resides in this inner region, the larger the polymer torque due to the vorticity perturbation. The large polymer torque then determines the amplitude of oscillation, or the vorticity wave, at later times when the flow and the polymer are two-way coupled and the disturbance aligns with the shear (3.29). Ultimately, as $\xi \rightarrow -\infty$, both diffusion in the solvent and the terms which were neglected in the original high Weissenberg number assumption should become important; these effects are now incorporated as we examine the long-time decay.

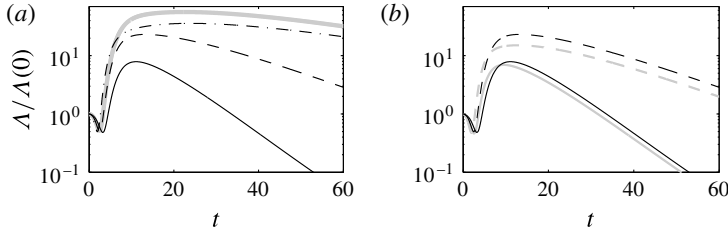


FIGURE 15. Long-time enstrophy evolutions of the Gaussian vortex. (a) Grey line, $R = 800$, $\beta = 0.8$, $W = 60$, such that $\mathcal{B} = 0.03$. Black lines, $R = 400$, $\beta = 0.8$; —, $W = 15$; ----, $W = 30$; — · —, $W = 60$. Note that the $R = 400$, $W = 30$ case also has $\mathcal{B} = 0.03$. (b) Black lines, $R = 400$, $\beta = 0.8$; grey lines, $R = 200$, $\beta = 0.8$; —, $W = 15$; ----, $W = 30$.

3.5. Long-time decay

The long-time evolution of the enstrophy of the Gaussian vortex is considered in figure 15 for a range of flow parameters. While the rate of amplification at earlier times was shown to be dependent on the elasticity, or the vorticity wavespeed $\sqrt{\mathcal{B}}$, the enstrophy decay rate does not retain this dependence; neither is the rate of decay dependent on the Reynolds number. At early times, during the amplification phase, the effects of solvent diffusion amounted to a damping in an oscillator equation. However, the results presented in figure 15(b) indicate that the long-time decay rate of the vortex is dictated by the Weissenberg number. The mechanics of this long-time decay are explored here.

It was remarked earlier that the high Weissenberg number approximation (3.9b) cannot be expected to hold when $t = O(W)$, since the reorientation of the phase fronts by the shear means that components of the base-state polymer stress other than T_{11} are no longer of secondary importance. More precisely, the magnitude of the terms neglected in the derivation of (3.9b) is dependent on the instantaneous wavenumber ratio, $\xi \equiv (k_r - \dot{\gamma}t)/\dot{\gamma}$, which was also used in § 3.4. Consider the original vorticity/polymer torque system (2.19b), rewritten in terms of ξ :

$$-\frac{d\hat{\omega}}{d\xi} = -\frac{\beta k_x^2}{R}(1 + \dot{\gamma}^2 \xi^2)\hat{\omega} + \frac{(1 - \beta)}{R}\hat{\chi}, \tag{3.33a}$$

$$-\frac{d\hat{\chi}}{d\xi} + \frac{1}{W}\hat{\chi} = -\frac{2\dot{\gamma}^2 \xi}{1 + \dot{\gamma}^2 \xi^2}\hat{\chi} - k_x^2 \left(T_{11} + 2T_{12}\dot{\gamma}\xi + \frac{1}{W}(1 + \dot{\gamma}^2 \xi^2) \right) \hat{\omega}. \tag{3.33b}$$

When $\xi = O(W)$, both $2T_{12}\dot{\gamma}\xi$ and $(1 + \dot{\gamma}^2 \xi^2)/W$ are of the same order as T_{11} , and cannot be neglected.

Since the long-time decay is determined by the elastic properties of the fluid, we define the scaled variable $\bar{\xi} \equiv \xi/W$, while $\{\bar{\omega}(\bar{\xi}), \bar{\chi}(\bar{\xi})\} = \{\hat{\omega}(\xi), \hat{\chi}(\xi)\}$. The system (3.33) becomes

$$-\frac{1}{W} \frac{d\bar{\omega}}{d\bar{\xi}} = -\frac{\beta k_x^2}{R}(1 + \dot{\gamma}^2 W^2 \bar{\xi}^2)\bar{\omega} + \frac{(1 - \beta)}{R}\bar{\chi}, \tag{3.34a}$$

$$-\frac{1}{W} \frac{d\bar{\chi}}{d\bar{\xi}} + \frac{1}{W}\bar{\chi} = -\frac{2\dot{\gamma}^2 W \bar{\xi}}{1 + \dot{\gamma}^2 W^2 \bar{\xi}^2}\bar{\chi} - k_x^2 \left(T_{11} + 2T_{12}\dot{\gamma}W\bar{\xi} + \frac{1}{W}(1 + \dot{\gamma}^2 W^2 \bar{\xi}^2) \right) \bar{\omega}. \tag{3.34b}$$

Assuming the Weissenberg number to be large, an asymptotic expansion is adopted:

$$\bar{\omega}(\bar{\xi}) = \bar{\omega}_0(\bar{\xi}) + W^{-1}\bar{\omega}_1(\bar{\xi}) + \dots, \quad (3.35a)$$

$$\bar{\chi}(\bar{\xi}) = W^2\bar{\chi}_0(\bar{\xi}) + W\bar{\chi}_1(\bar{\xi}) + \dots. \quad (3.35b)$$

If $W/R = O(1)$, then at leading order

$$0 = -\frac{\beta k_x^2}{R} \dot{\gamma}^2 \bar{\xi}^{-2} \bar{\omega}_0 + \frac{(1-\beta)}{R} \bar{\chi}_0, \quad (3.36a)$$

$$-\frac{d\bar{\chi}_0}{d\bar{\xi}} + \bar{\chi}_0 = -\frac{2}{\bar{\xi}} \bar{\chi}_0 - k_x^2 \left(\frac{T_{11}}{W} + 2T_{12} \dot{\gamma} \bar{\xi} + \dot{\gamma}^2 \bar{\xi}^2 \right) \bar{\omega}_0. \quad (3.36b)$$

The realignment of the wavevector by the mean shear, which generates large cross-stream gradients in the vorticity and enhances the rate of solvent diffusion, has rendered the effects of inertia unimportant. As a result, the leading-order vorticity equation (3.36a) is an instantaneous balance between the viscous torque in the solvent and the polymer torque. In the polymer evolution equation (3.36b) all terms are important.

The system (3.36) can be rewritten as a single equation for the vorticity:

$$\frac{d\bar{\omega}_0}{d\bar{\xi}} = \left(\frac{2(1-\beta)}{\beta \bar{\xi}^2} + \frac{2(1-\beta)}{\beta \bar{\xi}} + \frac{1}{\beta} \right) \bar{\omega}_0. \quad (3.37)$$

This equation is easily integrated, and the long-time evolution of a Fourier mode is therefore described by

$$\bar{\omega}_0(\bar{\xi}) = A_\infty \bar{\xi}^{2(1-\beta)/\beta} \exp \left(-\frac{2(1-\beta)}{\beta \bar{\xi}} + \frac{\bar{\xi}}{\beta} \right). \quad (3.38)$$

Therefore, the enstrophy at long times can be approximated by

$$\Lambda(t) \sim t^{4(1-\beta)/\beta} \exp \left(\frac{4W(1-\beta)}{\beta t} - \frac{2t}{W\beta} \right). \quad (3.39)$$

This expression is compared with the long-time behaviour obtained from numerical solution of the full equations (appendix A) for a single Fourier mode in figure 16, and good agreement is observed. There are several interesting features in the solution. (i) As $t \rightarrow \infty$, the decay rate of the vorticity perturbations is set by the retardation rate, $1/W\beta$. Decay at the retardation rate is associated with a rate-of-strain response to an applied stress. (ii) The role of the streamwise polymer stress, T_{11} , is altered from the splitting/amplification behaviours. In those regimes, the highly tensioned mean-flow streamlines provided a mechanism for wave propagation. However, here diffusion is sufficiently fast that the leading-order vorticity is instantaneously responsive to an applied polymer torque. Consequently, T_{11} leads to growth $\Lambda \sim \exp(4W(1-\beta)/\beta t)$. Its effects are weakened with time. (iii) There is also an algebraic growth, $\Lambda \sim t^{4(1-\beta)/\beta}$, although it is ultimately muted by the exponential decay. This algebraically growing component is due to the increasing effectiveness of the polymer shear stress, T_{12} , to generate polymer torque as the disturbance aligns with the shear.

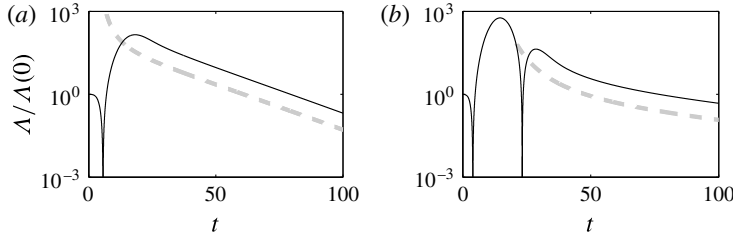


FIGURE 16. Enstrophy evolutions for individual Fourier modes, comparing the exact solution (black) to the long-time approximation of (3.39) (grey). (a) $R = 400$, $\beta = 0.8$, $W = 30$, $\mathbf{k}(0) = (1, 3)$; (b) $R = 1200$, $\beta = 0.7$, $W = 100$, $\mathbf{k}(0) = (1, 1)$.

3.6. Discussion

At large Weissenberg numbers, the evolution of the weak Gaussian vortex in homogeneous shear of an Oldroyd-B fluid departs significantly from the Newtonian behaviour. At early times, differences arise due to the large normal stress, T_{11} , and the kinematics of the polymer torque. The former provides a mechanism for vorticity to propagate as waves in the streamwise direction; the latter feeds tilting and stretching mechanisms for the generation of polymer torque. Together, these effects cause the vortex to split and amplify as it is tilted forward by the mean shear. Later, when the vortex is significantly deformed, the influence of inertia weakens and the long-time decay of the vortex is dictated by elastic effects. Large cross-stream gradients mean that both base-state polymer stresses are important, and the decay rate differs from the pure retardation which would be observed in the absence of shear.

The early-time dynamics were explained by adopting a high Weissenberg number approximation (3.9b). This assumption amounts to ignoring the effects of polymer relaxation, and taking the base-state stress to consist of T_{11} alone. In this limit vorticity disturbances propagate along the tensioned streamlines at a speed $\sqrt{\mathcal{B}} \equiv \sqrt{(1-\beta)T_{11}/R}$. These vorticity waves travel on top of the local base-flow velocity. They are confined to the streamwise direction, and are non-dispersive. In addition, a kinematic effect amplifies the polymer torque when the disturbance aligns with the mean shear – a mechanism we termed ‘reverse-Orr’ amplification. This mechanism, which is encapsulated by the coefficient \mathcal{S} in §3.4, generates torque at a point as advection realigns layers of varying polymer force. It operates on a time scale set by the shear, $\dot{\gamma}^{-1}$.

In §§3.3 and 3.4 the vortex splitting was demonstrated to be dominant when $k_x\sqrt{\mathcal{B}} \gg 1$, while amplification is most pronounced if $k_x\sqrt{\mathcal{B}} \ll 1$. The change in behaviour between these two limits can be understood by considering the relative number of vorticity waves that pass an observer moving at the local base-flow velocity within the shear time scale, $\dot{\gamma}^{-1}$:

$$n = \frac{\sqrt{\mathcal{B}}/\dot{\gamma}}{2\pi/k_x}. \tag{3.40}$$

If $k_x\sqrt{\mathcal{B}} \gg 1$ a large number of vorticity waves pass by: to the observer the amplification term ($\equiv \mathcal{S}\hat{\chi}$) appears highly oscillatory and is unable to generate a significant torque. Conversely, if $k_x\sqrt{\mathcal{B}} \ll 1$ the local polymer force field appears quasi-steady to the observer, and the kinematic amplification mechanism is most effective.

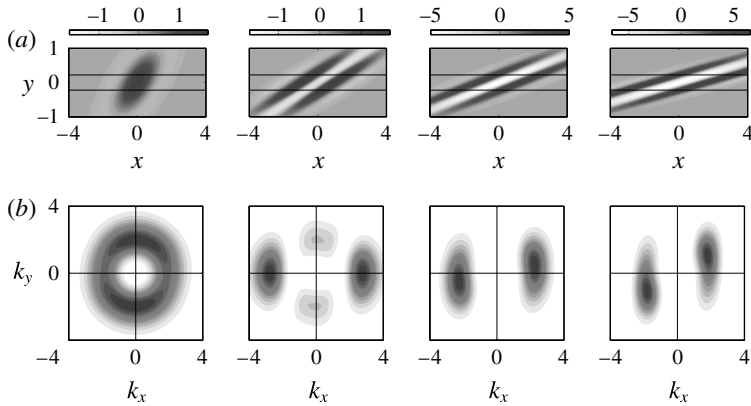


FIGURE 17. Evolution of a Gaussian vortex with $R = 1200$, $W = 100$, $\beta = 0.7$, snapshots extracted at $t = \{1, 3, 5, 7\}$. (a) Contours of spanwise vorticity; the locations of the critical layers, $y = \pm\lambda_c$, are indicated by the horizontal lines. Note that the aspect ratio is 2:1. (b) Spectral enstrophy density as a function of initial wavevector orientation.

In addition to the low frequency requirement, $k_x\sqrt{\mathcal{B}} \ll 1$, the matched asymptotic expansions in § 3.4 explicitly demonstrated that the amplification rate of a vorticity wave is a strong function of its initial orientation. While the amplification occurs when modes align with the shear (reverse-Orr), modes with an initial tilt against the shear, $k_r = k_y/k_x > 0$, are most strongly amplified once they become favourably aligned. The importance of the initial orientation is due to the fact that a significant polymer torque is generated when the wavefronts are almost vertical, $k_y(t)/k_x \sim 0$. In this region there is a one-way coupling from the flow perturbation to the polymer. This large torque then sets the amplification rate of the vorticity when the wavenumber satisfies the condition $k_y(t)/\dot{\gamma}k_x \lesssim 1/k_x\sqrt{\mathcal{B}}$, i.e. the outer solution from § 3.4. To relate this expression to the notion of travelling vorticity waves, the same condition can be written as

$$|k_y(t)| \gtrsim \lambda_c^{-1}, \tag{3.41}$$

where $\lambda_c \equiv \sqrt{\mathcal{B}}/\dot{\gamma}$ is a length scale that we term the ‘critical layer height’. This terminology is adopted from the stability literature (e.g. Drazin & Reid 1995), since it identifies points in the flow, $y = \pm\lambda_c$, where the base-flow velocity and the speed of vorticity-wave propagation are equal. A vorticity mode begins to experience amplification when its cross-stream length scale is of the order of the critical-layer height.

Snapshots of a vortex evolution which demonstrate these observations are provided in figure 17, along with the corresponding spectral enstrophy densities. As time advances, contours of the spectral enstrophy density indicate that the most amplified modes have an initial tilt against the shear, $k_r > 0$, in agreement with the arguments above. The critical layers in the flow, $y = \pm\lambda_c$, have been overlaid on the spanwise vorticity contours. As the disturbance starts to amplify (snapshots $t = \{5, 7\}$), the cross-stream length scale is of the order of the critical-layer height. Furthermore, the physical disturbance appears ‘pinned’ at the points $y = \pm\lambda_c$, where the base-flow velocity and either the left- or right-travelling vorticity wave combine to result in no overall motion.

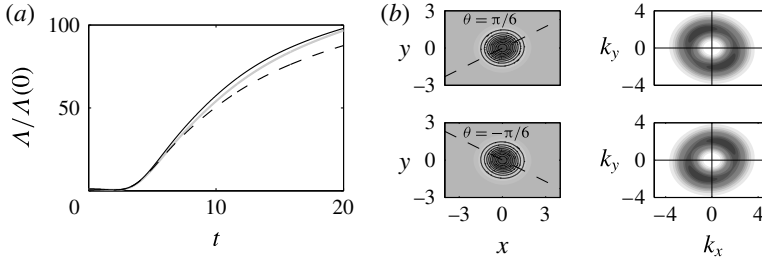


FIGURE 18. Evolution of a vortex without rotational symmetry, defined by (3.42) with $\delta = 0.05$. (a) Enstrophy evolution: —, $\theta = -\pi/6$; ---, $\theta = \pi/6$. The grey curve is the untitled reference case. (b) The initial condition for the tilted cases and the corresponding spectral enstrophy densities. The dashed lines identify the semi-major axes of the ellipses.

Finally, we comment briefly on the evolution of vortices without rotational symmetry. In examining the evolution of the axisymmetric Gaussian vortex, our analysis considered individual Fourier modes. The conclusions are therefore also applicable to other initial conditions. For the purposes of illustration, we consider the evolution of a slightly distorted vortex, without azimuthal symmetry:

$$\begin{bmatrix} u'(x', t = 0) \\ v'(x', t = 0) \end{bmatrix} = \alpha \begin{bmatrix} -y'(1 + \delta)^2 \\ x' \end{bmatrix} \exp(-(x'^2 + (1 + \delta)^2 y'^2)/l^2). \tag{3.42}$$

In the above expression, $\delta > 0$ and the primed coordinates are related to the original coordinate system through an anticlockwise rotation, $\mathbf{x}' = \mathbf{R}(\theta)\mathbf{x}$. The choice $0 < \theta < \pi/2$ gives the vortex an initial tilt against the shear, while $-\pi/2 < \theta < 0$ gives the vortex a favourable alignment with the shear. Example enstrophy evolutions for this initial condition for $\theta \in [-\pi/6, 0, \pi/6]$, $\delta = 0.05$ are provided in figure 18, alongside the initial condition and spectral enstrophy densities for the tilted cases. The enstrophy amplification differs slightly between the three cases under consideration; it is strongest when the initial condition is tilted against the shear. This is consistent with the discussion above and the analysis in § 3.4. The initial tilt against the shear corresponds to an increased effectiveness at generating polymer torque at early times, and, as a result, stronger amplification of vorticity in the reverse-Orr phase, when the disturbance is aligned with the shear.

4. Finite extensibility

The effects of finite extensibility of the polymer chains are now reintroduced. As remarked in § 2, the assumption that $L = \infty$ for the polymer chains is equivalent to a linear spring law. This simplification is known to be inaccurate in certain flow configurations. Examples include the unbounded growth of the polymer stress in extensional flows, and inaccurate assessment of hydrodynamic stability in parallel flows (Ray & Zaki 2014, 2015). Therefore, it is important to verify that the behaviour reported in § 3 is retained with a more realistic constitutive equation.

The influence of L on the energy and enstrophy evolution of the Gaussian vortex for a particular set of flow parameters is reported in figure 19. For very large polymer extensibility, $L = 1000$, the Oldroyd-B results are recovered as anticipated. As L is reduced, $L = \{100, 50\}$, the rate of enstrophy amplification is altered slightly, but the qualitative behaviour remains unchanged. However, the decay sets in earlier and at

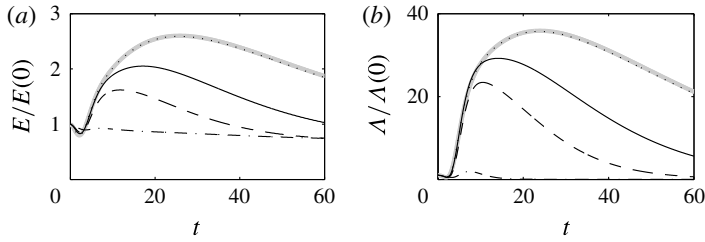


FIGURE 19. Influence of L on (a) energy and (b) enstrophy evolution of the Gaussian vortex. Here $R = 400$, $W = 60$, $\beta = 0.8$: \cdots , $L = 1000$; --- , $L = 100$; - - - , $L = 50$; $\text{---}\cdot\text{---}$, $L = 10$. The thick grey lines are the Oldroyd-B results.

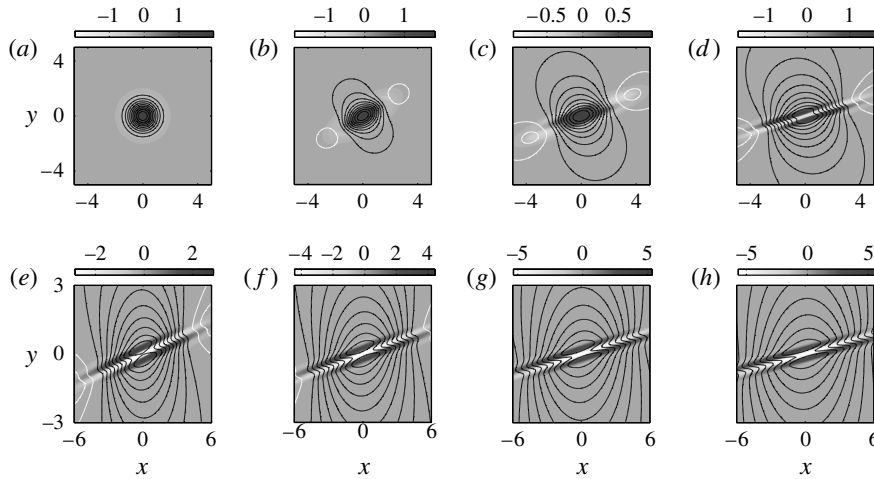


FIGURE 20. Time evolution of the vorticity (shading) and streamfunction (lines) for the Gaussian vortex in a FENE-P fluid with $L = 100$. Here, $R = 400$, $W = 60$ and $\beta = 0.8$. The instantaneous fields correspond to $t = \{0, 1, 2, \dots, 7\}$. Note the change in aspect ratio for $t \geq 4$.

a higher rate than the Oldroyd-B results. For the smallest extensibility, $L = 10$, the influence of the polymer on the flow dynamics diminishes; only a small amplification of Λ is observed prior to the onset of decay. The practical relevance of drag-reduced flows and elasto-inertial turbulence focuses our interest on values of $L = O(100)$.

The effect of finite extensibility on disturbance evolution is examined further in figure 20. Snapshots showing contours of the spanwise vorticity and the streamfunction are reported, and should be compared to those appearing in figure 4 which are the analogous Oldroyd-B results. The time series focuses on the initial amplification phase, where the FENE-P evolution appears similar to the Oldroyd-B fluid. In particular, the short-time vortex splitting is observed, as is the subsequent amplification in long stripes. These results are in accord with the enstrophy evolution reported in figure 19, and confirm that the finite polymer extensibility does not alter the qualitative behaviour of the vorticity field and its amplification.

The influence of L on the decay of the disturbance is much more pronounced, and merits further discussion. In the context of the linear perturbation equations, the finite

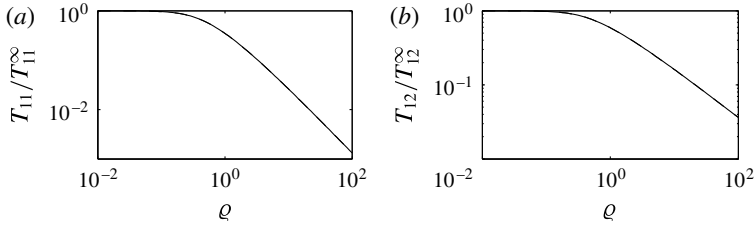


FIGURE 21. Influence of finite extensibility on the base-state polymer stresses: (a) normal stress and (b) shear stress. The superscript ∞ indicates the Oldroyd-B result.

extensibility influences the dynamics through (i) an altered base-state stress tensor and (ii) an additional class of stress perturbations.

The influence of finite polymer extensibility on the base-state stresses has been examined by Ray & Zaki (2014), and a brief overview is provided here. Those authors show that the ratios of the FENE-P stresses to the Oldroyd-B values are

$$\frac{T_{11}}{T_{11}^\infty} = \frac{1}{F(\rho)^2}, \quad \frac{T_{12}}{T_{12}^\infty} = \frac{1}{F(\rho)}, \tag{4.1a,b}$$

where the Peterlin function, F , is expressed in terms of $\rho \equiv \dot{\gamma}\zeta/L$ (see appendix A). The two ratios (4.1) are reported in figure 21. There is a significant reduction of both base-state stresses when $\rho \gg 1$. However, for the flow parameters of interest here, $\rho \lesssim 1$, and thus $F(\rho) \sim 1$. As a result, the Oldroyd-B scaling remains, $T_{11} = O(W\dot{\gamma}^2)$, $T_{12} = O(\dot{\gamma})$, and the short-time dynamics retain the same features as the Oldroyd-B results.

For an Oldroyd-B fluid, the role of the base-state stresses is to weaken the enstrophy decay rate (see § 3.5). In particular the normal stress resulted in an exponentially amplifying term and the polymer shear-stress caused an algebraic amplification. Therefore, the weaker base-state stresses for FENE-P fluids go some way towards explaining the trend seen in figure 19. However, the dominant contribution to decay in (3.39) is set by the retardation rate. The retardation rate is proportional to the polymer relaxation rate which, in the FENE-P fluid, increases due to a new form of stress perturbation. This additional stress perturbation arises from the nonlinearity of the spring law, and was discussed in connection with (2.7):

$$\tau_{ij} = \frac{F}{W} \left(c_{ij} + \underbrace{\frac{1}{L^2 - C_{ll}} c_{ij} c_{kk}}_{\mathcal{N}} \right). \tag{4.2}$$

The nonlinear springs become increasingly stiff as the polymer chains approach their extensibility limit, and this is reflected in the linear theory through the dependence on c_{kk} . Contours of c_{kk}/L^2 , extracted from a vortex evolution in a FENE-P fluid, are reported in figure 22. The snapshots include both the amplification period ($t = \{4, 5, 6, 7\}$) and the interval during which the enstrophy is decaying ($t = \{24, 28, 32, 36\}$). The polymers become significantly stretched at early times. There is a thin region of strong positive stretch, $c_{kk}/L^2 > 0$, surrounded by regions where the polymer is compressed, $c_{kk}/L^2 < 0$. At long time, the region of positive stretch remains despite the decay of energy and enstrophy. The stretching is isolated in a very narrow region, and is reminiscent of flow structures observed in nonlinear

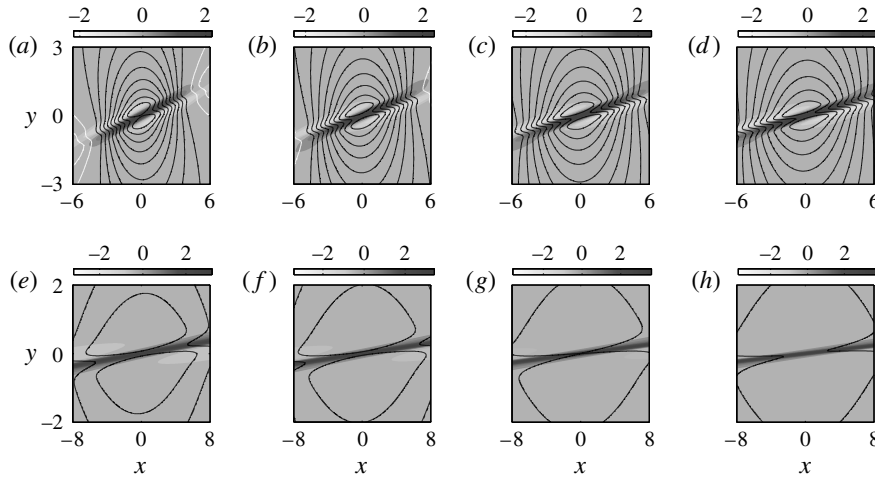


FIGURE 22. Time evolution of the trace of the conformation tensor, c_{kk}/L^2 (shading), with the streamfunction overlaid (lines) for the Gaussian vortex in a FENE-P fluid with $L=100$. Here, $R=400$, $W=60$ and $\beta=0.8$. The instantaneous fields correspond to $t = \{4, 5, 6, 7\}$ (a–d) and $t = \{24, 28, 32, 36\}$ (e–h). Note the change in aspect ratio.

simulations of inertial polymer flows (Dubief *et al.* 2013; Agarwal *et al.* 2014; Wang *et al.* 2014).

The mechanism behind the flow localization can be explained by contracting the polymer conformation (2.6c) to obtain the evolution of c_{ii} ,

$$\left[\frac{d}{dt} + \frac{F}{W} \left(1 + \frac{C_{jj}}{L^2 - C_{kk}} \right) \right] \hat{c}_{ii} = 2C_{ij}\hat{e}_{ij} + 2E_{ij}\hat{c}_{ij}, \tag{4.3}$$

where $\hat{e}_{ij} = (1/2)(ik_j\hat{u}_i + ik_i\hat{u}_j)$ is the perturbation rate-of-strain tensor. Note that the polymer is only stretched by the straining component of the flow. Contours of the two terms on the right-hand side of (4.3) are provided in figure 23 and correspond to four of the snapshots of c_{kk}/L^2 reported in figure 22. The first of these two terms, namely $2C_{ij}\hat{e}_{ij}$, is the action of the straining from the perturbation flow field on the base-state polymer stretch. It acts to compress the polymer between the two co-rotating vortices. The second term, $2E_{ij}\hat{c}_{ij}$, describes the stretching of the polymer due to straining by the mean flow. This term is dominant throughout the vortex evolution and stretches the polymer in a thin region, or sheet.

In summary, the influence of finite extensibility becomes progressively more pronounced during the evolution of the Gaussian vortex. In the early amplification phase the behaviour remains qualitatively similar to the Oldroyd-B results, largely due to dominance of the base-state streamwise stress. However, the significant stretching of the polymer in an isolated region initiates a more rapid polymer relaxation rate, and causes an earlier onset of enstrophy decay.

5. Conclusions

The evolution of spanwise vorticity perturbations in dilute polymer solutions has been studied using the model problem of a Gaussian vortex superposed onto a homogeneous shear flow. The analysis identified two behaviours unique to viscoelastic

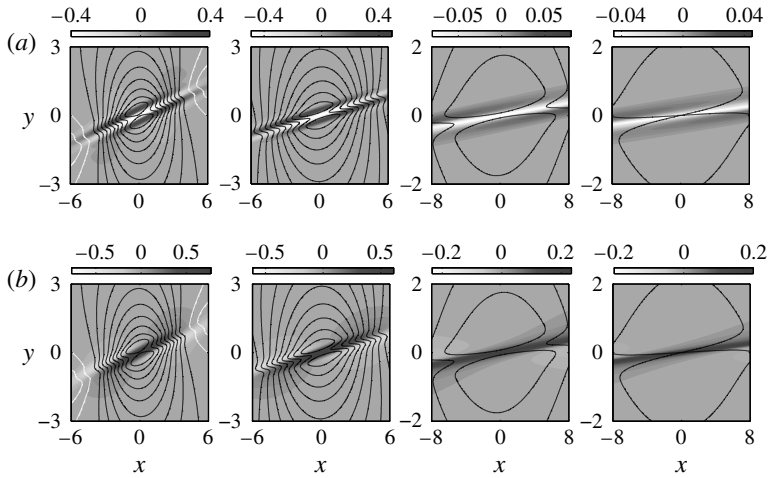


FIGURE 23. Snapshots of the two terms on the right-hand side of (4.3) (shading) with the streamfunction overlaid (lines) for the Gaussian vortex in a FENE-P fluid with $L = 100$, $R = 400$, $W = 60$, $\beta = 0.8$. The instantaneous fields correspond to $t = \{4, 6, 24, 32\}$. (a) $2C_{ij}\hat{e}_{ij}/L^2$; (b) $2E_{ij}\hat{c}_{ij}/L^2$. Note the changing aspect ratio.

fluids: (i) the tensioned mean-flow streamlines support streamwise vorticity wave propagation; (ii) the vorticity amplifies as the disturbance is aligned with the shear. These two effects were explained using the linear perturbation equations for Oldroyd-B fluids.

In the present set-up, the vorticity wave propagation led to the splitting of the Gaussian vortex at early times. The behaviour is most pronounced for high elasticity, or equivalently small-scale disturbances in strong shear, where the waves travel much faster than the rate at which an eddy is deformed by the mean flow.

For weak elasticity but high Weissenberg number, the splitting is still observed at early times. However, there is an amplification of spanwise vorticity as the disturbance is reoriented in the direction of the shear by the base flow. The amplification is due to a kinematic mechanism for the growth of the polymer torque. This mechanism behaves somewhat analogously to Orr amplification in Newtonian fluids. However, the Orr amplification requires a tilt in the perturbation streamlines against the shear, while the torque amplification has the opposite behaviour, and amplification occurs during alignment with the shear.

Calculations of vortex evolutions with the more realistic FENE-P model showed similar qualitative behaviour. However, for small polymer extensibility the onset of decay occurs sooner, and its rate is more rapid. This effect is due to a faster retardation rate driven by a new form of stress perturbation, which is proportional to net stretching of the polymer chains, and is a result of their nonlinearity. Straining by the base flow results in significant stretching of the polymer in an isolated region, or a sheet.

The present analysis has identified a variety of new dynamical behaviours for small spanwise vorticity perturbations in viscoelastic shear flows, and demonstrated a new mechanism by which the vorticity can amplify. Despite the idealized flow configuration and choice of initial disturbance, the results show some qualitative similarities with flow structures observed in more complex configurations, such as

nonlinear EIT (Dubief *et al.* 2013), and in transitional viscoelastic channel flow (Agarwal *et al.* 2014). Finally, we note that the dependence of the dynamics on the elasticity, $E^* = W(1 - \beta)/R \equiv \zeta v_p/l^2$, is equivalent to a dependence on the length scale of the disturbance in a particular fluid. Consequently, both wave propagation and amplification may be observed at different length scales in any given flow.

Acknowledgement

This work is sponsored by the Engineering and Physical Sciences Research Council and the National Science Foundation.

Appendix A. Further details on theoretical formulation

A.1. Polymer torque

In the main body of the paper the terminology ‘polymer torque’ is adopted in reference to the curl of the polymer force. The purpose of this section is to demonstrate the connection between $\boldsymbol{\chi} \equiv \nabla \wedge \mathbf{f}$ and the actual torque exerted by the polymer stresses on a fluid element. The presentation is similar to that given by Saffman (1992) in relation to vorticity and angular momentum.

Consider an infinitesimal fluid element with volume δV . The torque exerted on this element about its centroid by the polymer stresses is

$$\delta \boldsymbol{\zeta} = \mu_p \int_{\delta V} (\delta \mathbf{x} \wedge \delta \mathbf{f}) \, dV, \quad (\text{A } 1)$$

where $\mu_p f_i = \mu_p \partial \tau_{ij} / \partial x_j$ is the perturbation polymer force per unit volume.

The difference in the force across the fluid element is

$$\begin{aligned} \delta f_i &= \frac{\partial f_i}{\partial x_j} \delta x_j \\ &= \frac{1}{2} \left(\frac{\partial f_i}{\partial x_j} + \frac{\partial f_j}{\partial x_i} \right) \delta x_j + \frac{1}{2} \left(\frac{\partial f_i}{\partial x_j} - \frac{\partial f_j}{\partial x_i} \right) \delta x_j \\ &= \frac{1}{2} \left(\frac{\partial f_i}{\partial x_j} + \frac{\partial f_j}{\partial x_i} \right) \delta x_j - \frac{1}{2} \epsilon_{ijk} \chi_k \delta x_j, \end{aligned} \quad (\text{A } 2)$$

where $\boldsymbol{\chi} \equiv \nabla \wedge \mathbf{f}$ is defined in the text as the ‘polymer torque’. Equation (A 1) now reads

$$\begin{aligned} \delta \zeta_i &= \frac{1}{2} \mu_p \int_{\delta V} \epsilon_{ijk} \delta x_j \left(\frac{\partial f_k}{\partial x_l} + \frac{\partial f_l}{\partial x_k} \right) \delta x_l \, dV - \frac{1}{2} \mu_p \int_{\delta V} \epsilon_{ijk} \epsilon_{klm} \delta x_j \chi_m \delta x_l \, dV \\ &= \frac{1}{2} \mu_p \int_{\delta V} \epsilon_{ijk} \delta x_j \left(\frac{\partial f_k}{\partial x_l} + \frac{\partial f_l}{\partial x_k} \right) \delta x_l \, dV + \frac{1}{2} \mu_p \int_{\delta V} (\delta x_k \delta x_l \delta_{ij} - \delta x_i \delta x_j) \chi_j \, dV. \end{aligned} \quad (\text{A } 3)$$

As $\delta V \rightarrow 0$ we may write

$$\delta \zeta_i = \frac{1}{2} \mu_p \epsilon_{ijk} \left(\frac{\partial f_k}{\partial x_l} + \frac{\partial f_l}{\partial x_k} \right) \int_{\delta V} \delta x_j \delta x_l \, dV + \frac{1}{2} v_p I_{ij} \chi_j, \quad (\text{A } 4)$$

where $I_{ij} = \rho \int_{\delta V} (\delta x_k \delta x_l \delta_{ij} - \delta x_i \delta x_j) \, dV$ is the inertia tensor of the fluid element. If our fluid element is a sphere, then the first term on the right-hand side of (A 4) vanishes, and

$$\delta \boldsymbol{\zeta} = \frac{1}{2} v_p I \boldsymbol{\chi}. \quad (\text{A } 5)$$

The ‘polymer torque’, $\boldsymbol{\chi}$, is therefore proportional to the physical torque, $\delta \boldsymbol{\zeta}$, exerted on a spherical fluid element by the polymer stresses.

A.2. Base-state conformation tensor

Expressions for the base-state conformation tensor were provided in (2.12) for an Oldroyd-B fluid. The corresponding FENE-P values are

$$C_{11} = \frac{1}{F} \left(1 + \frac{2\dot{\gamma}^2 \zeta^2}{F^2} \right), \quad C_{12} = \frac{\dot{\gamma} \zeta}{F^2}, \quad C_{22} = C_{33} = \frac{1}{F}, \quad (\text{A } 6a-c)$$

where F , the Peterlin function, can be written in terms of the variable $\varrho \equiv \dot{\gamma} \zeta / L$ (Sureshkumar, Beris & Handler 1997):

$$F(\varrho) = \frac{\sqrt{6}\varrho}{2 \sinh(\vartheta/3)}, \quad \text{where } \vartheta = \sinh^{-1}(3\sqrt{6}\varrho/2). \quad (\text{A } 6d)$$

A.3. Linear equations in Fourier space

The majority of results presented in this paper were computed numerically by time-advancement of the Fourier coefficients in primitive variables. These equations are presented here.

The momentum equations in Fourier space read

$$\frac{d\hat{u}}{dt} = -\dot{\gamma}\hat{v} + \frac{2k_x^2\dot{\gamma}}{|\mathbf{k}(t)|^2}\hat{v} - \frac{\beta|\mathbf{k}(t)|^2}{R}\hat{u} + \frac{(1-\beta)}{R} \left(ik_x\hat{\tau}_{11} + ik_y(t)\hat{\tau}_{12} - \frac{ik_xk_ik_j}{|\mathbf{k}(t)|^2}\hat{\tau}_{ij} \right), \quad (\text{A } 7a)$$

$$\frac{d\hat{v}}{dt} = \frac{2k_xk_y(t)\dot{\gamma}}{|\mathbf{k}(t)|^2}\hat{v} - \frac{\beta|\mathbf{k}(t)|^2}{R}\hat{v} + \frac{(1-\beta)}{R} \left(ik_x\hat{\tau}_{12} + ik_y(t)\hat{\tau}_{22} - \frac{ik_y(t)k_ik_j}{|\mathbf{k}(t)|^2}\hat{\tau}_{ij} \right), \quad (\text{A } 7b)$$

where the continuity equation, $k_x\hat{u} + k_y(t)\hat{v} = 0$, is satisfied implicitly since it has been invoked to rewrite the pressure:

$$\hat{p} = \frac{2ik_x\dot{\gamma}}{|\mathbf{k}(t)|^2}\hat{v} + \frac{(1-\beta)k_ik_j}{R|\mathbf{k}(t)|^2}\hat{\tau}_{ij}. \quad (\text{A } 8)$$

The Fourier coefficients of the polymer stress are related to the polymer conformation through

$$\hat{\tau}_{ij} = \frac{F}{W} \left(\hat{c}_{ij} + \frac{F}{L^2 - 3} C_{ij} \hat{c}_{kk} \right). \quad (\text{A } 9)$$

The coefficients of the polymer conformation evolve according to

$$\frac{d\hat{c}_{11}}{dt} = (2ik_xC_{11} + 2ik_y(t)C_{12})\hat{u} + 2\dot{\gamma}\hat{c}_{12} - \hat{\tau}_{11}, \quad (\text{A } 10a)$$

$$\frac{d\hat{c}_{12}}{dt} = ik_xC_{11}\hat{v} + ik_y(t)C_{22}\hat{u} + \dot{\gamma}\hat{c}_{22} - \hat{\tau}_{12}, \quad (\text{A } 10b)$$

$$\frac{d\hat{c}_{22}}{dt} = (2ik_xC_{12} + 2ik_y(t)C_{22})\hat{v} - \hat{\tau}_{22}, \quad (\text{A } 10c)$$

$$\frac{d\hat{c}_{33}}{dt} = -\hat{\tau}_{33}. \quad (\text{A } 10d)$$

The Fourier coefficients are advanced in time with an explicit Adams–Bashforth scheme. Integral quantities of interest, such as the perturbation energy and enstrophy,

are computed in spectral space using Parseval's theorem. The inversion integral (2.17) is computed with a direct Riemann sum to obtain fields in physical space.

REFERENCES

- AGARWAL, A., BRANDT, L. & ZAKI, T. A. 2014 Linear and nonlinear evolution of a localized disturbance in polymeric channel flow. *J. Fluid Mech.* **760**, 278–303.
- DEL ÁLAMO, J. C. & JIMÉNEZ, J. 2006 Linear energy amplification in turbulent channels. *J. Fluid Mech.* **559**, 205–213.
- AZAIÉZ, J. & HOMSY, G. M. 1994 Linear stability of free shear flow of viscoelastic liquids. *J. Fluid Mech.* **268**, 37–69.
- BAYLY, B. J. 1986 Three-dimensional instability of elliptical flow. *Phys. Rev. Lett.* **57** (17), 2160–2163.
- BENDER, C. M. & ORSZAG, S. A. 1978 *Advanced Mathematical Methods for Scientists and Engineers*, 1st edn. McGraw-Hill.
- BIRD, R. B., ARMSTRONG, R. C. & HASSAGER, O. 1987 *Dynamics of Polymeric Liquids*, 2nd edn. vol. 1. Wiley.
- BUTLER, K. M. & FARRELL, B. F. 1992 Optimal perturbations in viscous shear flow. *Phys. Fluids* **4**, 1637–1650.
- CADOT, O. & KUMAR, S. 2000 Experimental characterization of viscoelastic effects on two- and three-dimensional shear instabilities. *J. Fluid Mech.* **416**, 151–172.
- DIMITROPOULOS, C. D., SURESHKUMAR, R., BERIS, A. N. & HANDLER, R. A. 2001 Budgets of Reynolds stress, kinetic energy and streamwise enstrophy in viscoelastic turbulent channel flow. *Phys. Fluids* **13**, 1016.
- DOERING, C. R., ECKHARDT, B. & SCHUMACHER, J. 2006 Failure of energy stability in Oldroyd-B fluids at arbitrarily low Reynolds numbers. *J. Non-Newtonian Fluid Mech.* **135**, 92–96.
- DRAZIN, P. & REID, W. H. 1995 *Hydrodynamic Stability*. Cambridge University Press.
- DUBIEF, Y., TERRAPON, V. E. & SORIA, J. 2013 On the mechanism of elasto-inertial turbulence. *Phys. Fluids* **25** (11), 110817.
- DUBIEF, Y., TERRAPON, V. E., WHITE, C. M., SHAQFEH, E. S. G., MOIN, P. & LELE, S. K. 2005 New answers on the interaction between polymers and vortices in turbulent flows. *Flow Turbul. Combust.* **74** (4), 311–329.
- DUBIEF, Y., WHITE, C. M., TERRAPON, V. E., SHAQFEH, E. S. G., MOIN, P. & LELE, S. K. 2004 On the coherent drag-reducing and turbulence-enhancing behaviour of polymers in wall flows. *J. Fluid Mech.* **514**, 271–280.
- FARRELL, B. 1987 Developing disturbances in shear. *J. Atmos. Sci.* **44**, 2191–2199.
- GRAHAM, M. D. 2014 Drag reduction and the dynamics of turbulence in simple and complex fluids. *Phys. Fluids* **26**, 101301.
- GROISMAN, A. & STEINBERG, V. 2000 Elastic turbulence in a polymer solution flow. *Nature* **405**, 53–55.
- HAJ-HARIRI, H. & HOMSY, G. M. 1997 Three-dimensional instability of viscoelastic elliptic vortices. *J. Fluid Mech.* **353**, 357–381.
- HARDER, K. J. & TIEDERMAN, W. G. 1991 Drag reduction and turbulent structure in two-dimensional channel flows. *Phil. Trans. R. Soc. Lond. A* **336** (1640), 19–34.
- HINCH, E. J. 1977 Mechanical models of dilute polymer solutions in strong flows. *Phys. Fluids* **20** (10), S22.
- HODA, N., JOVANOVIĆ, M. R. & KUMAR, S. 2008 Energy amplification in channel flows of viscoelastic fluids. *J. Fluid Mech.* **601**, 407–424.
- HODA, N., JOVANOVIĆ, M. R. & KUMAR, S. 2009 Frequency responses of streamwise-constant perturbations in channel flows of Oldroyd-B fluids. *J. Fluid Mech.* **625**, 411–434.
- JIMÉNEZ, J. 2013 How linear is wall-bounded turbulence? *Phys. Fluids* **25** (11), 110814.
- JIN, S. & COLLINS, L. R. 2007 Dynamics of dissolved polymer chains in isotropic turbulence. *New J. Phys.* **9**, 360.
- JOVANOVIĆ, M. R. & KUMAR, S. 2010 Transient growth without inertia. *Phys. Fluids* **22**, 023101.

- JOVANOVIĆ, M. R. & KUMAR, S. 2011 Nonmodal amplification of stochastic disturbances in strongly elastic channel flows. *J. Non-Newtonian Fluid Mech.* **166**, 755–778.
- KIM, K., LI, C.-F., SURESHKUMAR, R., BALACHANDAR, S. & ADRIAN, R. J. 2007 Effects of polymer stresses on eddy structures in drag-reduced turbulent channel flow. *J. Fluid Mech.* **584**, 281–299.
- KUMAR, S. & HOMSY, G. M. 1999 Direct numerical simulation of hydrodynamic instabilities in two- and three-dimensional viscoelastic free shear layers. *J. Non-Newtonian Fluid Mech.* **83**, 249–276.
- KUPFERMAN, R. 2005 On the linear stability of plane Couette flow for an Oldroyd-B fluid and its numerical approximation. *J. Non-Newtonian Fluid Mech.* **127**, 169–190.
- LAGNADO, R. R. & SIMMEN, J. A. 1993 The three-dimensional instability of elliptical vortices in a viscoelastic fluid. *J. Non-Newtonian Fluid Mech.* **50**, 29–44.
- LANDAHL, M. T. 1980 A note on an algebraic instability of inviscid parallel shear flows. *J. Fluid Mech.* **98**, 243–251.
- LIEU, B. K., JOVANOVIĆ, M. R. & KUMAR, S. 2013 Worst-case amplification of disturbances in inertialess Couette flow of viscoelastic fluids. *J. Fluid Mech.* **723**, 232–263.
- LUCHIK, T. S. & TIEDERMAN, W. G. 1988 Turbulent structure in low-concentration drag-reducing channel flows. *J. Fluid Mech.* **190**, 241–263.
- MIN, T., YUL YOO, J., CHOI, H. & JOSEPH, D. D. 2003 Drag reduction by polymer additives in a turbulent channel flow. *J. Fluid Mech.* **486**, 213–238.
- MOFFATT, H. K. 1967 The interaction of turbulence with strong wind shear. In *Atmospheric Turbulence and Radio Wave Propagation* (ed. A. M. Yaglom & V. I. Tatarski), pp. 139–156. Moscow.
- PAGE, J. & ZAKI, T. A. 2014 Streak evolution in viscoelastic Couette flow. *J. Fluid Mech.* **742**, 520–551.
- PAN, L., MOROZOV, A., WAGNER, C. & ARRATIA, P. E. 2013 Nonlinear elastic instability in channel flows at low Reynolds numbers. *Phys. Rev. Lett.* **110**, 174502.
- PTASINSKI, P. K., BOERSMA, B. J., NIEUWSTADT, F. T. M., HULSEN, M. A., VAN DEN BRULE, B. H. A. A. & HUNT, J. C. R. 2003 Turbulent channel flow near maximum drag reduction: simulations, experiments and mechanisms. *J. Fluid Mech.* **490**, 251–291.
- RALLISON, J. M. & HINCH, E. J. 1995 Instability of a high-speed submerged elastic jet. *J. Fluid Mech.* **288**, 311–324.
- RAY, P. K. & ZAKI, T. A. 2014 Absolute instability in viscoelastic mixing layers. *Phys. Fluids* **26** (1), 014103.
- RAY, P. K. & ZAKI, T. A. 2015 Absolute/convective instability of planar viscoelastic jets. *Phys. Fluids* **27**, 014110.
- ROBINSON, S. K. 1991 Coherent motions in the turbulent boundary layer. *Annu. Rev. Fluid Mech.* **23**, 601–639.
- SAFFMAN, P. G. 1992 *Vortex Dynamics*. Cambridge University Press.
- SAMANTA, D. S., DUBIEF, Y., HOLZNER, H., SCHÄFER, C., MOROZOV, A. N., WAGNER, C. & HOF, B. 2013 Elasto-inertial turbulence. *Proc. Natl Acad. Sci. USA* **110**, 10557–10562.
- SURESHKUMAR, R., BERIS, A. N. & HANDLER, R. A. 1997 Direct numerical simulation of the turbulent channel flow of a polymer solution. *Phys. Fluids* **9**, 743–755.
- TERRAPON, V. E., DUBIEF, Y. & SORIA, J. 2014 On the role of pressure in elasto-inertial turbulence. *J. Turbul.* **16** (1), 26–43.
- TOWNSEND, A. A. 1976 *The Structure of Turbulent Shear Flow*, 2nd edn. Cambridge University Press.
- WALKER, D. T. & TIEDERMAN, W. G. 1990 Turbulent structure in a channel flow with polymer injection at the wall. *J. Fluid Mech.* **218**, 377–403.
- WANG, S.-N., GRAHAM, M. D., HAHN, F. J. & XI, L. 2014 Time-series and extended Karhunen–Loève analysis of turbulent drag reduction in polymer solutions. *AIChE J.* **60** (4), 1460–1475.
- WHITE, C. M. & MUNGAL, M. G. 2008 Mechanics and prediction of turbulent drag reduction with polymer additives. *Annu. Rev. Fluid Mech.* **40**, 235–256.

- XI, L. & GRAHAM, M. D. 2010 Turbulent drag reduction and multistage transitions in viscoelastic minimal flow units. *J. Fluid Mech.* **647**, 421–452.
- XI, L. & GRAHAM, M. D. 2012 Intermittent dynamics of turbulence hibernation in Newtonian and viscoelastic minimal channel flows. *J. Fluid Mech.* **693**, 433–472.
- ZHANG, M., LASHGARI, I., ZAKI, T. A. & BRANDT, L. 2013 Linear stability analysis of channel flow of viscoelastic Oldroyd-B and FENE-P fluids. *J. Fluid Mech.* **737**, 249–279.